


# Franz-Keldysh and Stark Effects in Two-Dimensional Metal Halide Perovskites

Kameron R. Hansen<sup>1,\*</sup>, C. Emma McClure,<sup>2</sup> John S. Colton<sup>2,†</sup> and Luisa Whittaker-Brooks<sup>1,‡</sup>

<sup>1</sup>*Department of Chemistry, University of Utah, Salt Lake City, Utah 84112, USA*

<sup>2</sup>*Department of Physics and Astronomy, Brigham Young University, Provo, Utah 84602, USA*

 (Received 21 September 2021; revised 22 December 2021; accepted 2 February 2022; published 7 April 2022)

The established theory of a two-dimensional (2D) Wannier exciton in a uniform electric field is used to analyze the electroabsorption response of an archetypal 2D metal halide perovskite (MHP), phenethylammonium lead iodide. The high level of agreement between the electroabsorption simulation and measurement allows for a deepened understanding of the redshift of exciton energy, according to the quadratic Stark effect, and the continuum wave function leaking, according to the Franz-Keldysh effect. We find the field dependency of each of these effects to be rich with information, yielding measurements of the exciton Bohr radius, transition dipole moment, polarizability, and reduced effective mass of the exciton. Most importantly, the band-gap energy and exciton binding energy are unambiguously determined with  $1\sigma$  variance of 4 meV. The high precision of these new measurement methods opens the opportunity for determining the influence of chemical and environmental factors on the optoelectronic properties of MHPs, which would enable the fabrication of highly efficient and reproducible light-harvesting and light-emitting optoelectronic devices.

DOI: [10.1103/PRXEnergy.1.013001](https://doi.org/10.1103/PRXEnergy.1.013001)

## I. INTRODUCTION

Metal halide perovskites (MHPs) are the star optoelectronic materials of this decade and show exciting promise for photovoltaic and light-emitting applications [1–3]. In their two-dimensional (2D) form, 2D MHPs host stable excitons that are broadly viewed as analogous to those in inorganic quantum wells based on III-V semiconductors, such as GaAs-AlGaAs [4,5]. However, unlike III-V quantum wells, which are grown with expensive epitaxial techniques to target defect-free crystals, 2D MHPs naturally crystallize into a heterostructure consisting of alternating organic-inorganic layers. Both the organic and inorganic components of the lattice impart distinct effects on the exciton. For example, the low-dielectric organic layer enhances the Coulomb interaction and causes an image charge effect, resulting in far greater exciton binding energies [6,7]. In a similar vein, phonons within the inorganic layer couple to the exciton states, resulting in the coexistence of multiple exciton-polarons with distinct

phonon coherences [8,9]. The result is a unique, tightly bound, highly polaronic, and moderately delocalized exciton that is becoming the focus of significant research efforts, both from fundamental and applied perspectives [10–12].

While the assembly of 2D MHPs into photovoltaics, light-emitting diodes (LEDs), lasers, and other optoelectronic devices has thus far been promising [13–16], these materials have yet to achieve the applied successes of their all-inorganic quantum well counterparts. To translate the unique photophysical properties of the excitons present in 2D MHPs into successful devices, a deeper understanding of the underlying absorption features and an understanding of how to tune their optoelectronic properties are needed. Unfortunately, the same lattice effects (e.g., dynamic disorder and phonon coupling) that give excitons in 2D MHPs their unique character and defect-tolerant properties also result in spectral structures which are difficult to interpret. Nowhere is this more evident than with the difficulty in measuring exciton binding energies ( $E_B$ ) for both 2D and three-dimensional (3D) MHPs, a parameter of great importance for solar cell engineering, as it determines the ratio of excitons to free carriers, and for LED engineering, as it strongly dictates electroluminescence quantum efficiency [17]. For example, taking the well-known 2D MHPs phenethylammonium lead iodide (PEA<sub>2</sub>PbI<sub>4</sub>) and butylammonium lead iodide (BA<sub>2</sub>PbI<sub>4</sub>) as case studies, state-of-the-art techniques for measuring  $E_B$  in 2D MHPs, namely, absorption, photoluminescence excitation,

\*kameron.hansen@utah.edu

†john\_colton@byu.edu

‡luisa.whittaker@utah.edu

*Published by the American Physical Society under the terms of the Creative Commons Attribution 4.0 International license. Further distribution of this work must maintain attribution to the author(s) and the published article's title, journal citation, and DOI.*

electroabsorption, and low- and high-field magnetoabsorption at liquid helium temperatures have thus far led to  $E_B$  values ranging from 190 to 490 meV [18–23]. While some of this variance is caused by differences in the organic molecule, sample thickness, dielectric environment, and morphology, a significant portion of the variance originates from differing interpretations of band-edge absorption features and assumptions that are intrinsic to the measurement techniques. For theoretical and applied research directions within the MHP field to move forward, it is critical to develop high-confidence model-independent measurement methods that are precise and reproducible.

In pursuit of such measurements and a clear understanding of the optoelectronic properties in 2D MHPs, we are motivated to turn to the technique that has been the most significant in advancing the fundamental understanding of III-V quantum wells, namely, electroabsorption spectroscopy (EA). EA measures the difference in a material's absorption spectrum,  $A$ , with and without an applied field,  $F$ , as follows:

$$\Delta A = A(F) - A(F = 0). \quad (1)$$

In the 1980s, seminal EA studies by the groups of Bastard, Mendez, and Miller [24–28], built on the theory of Dow and Redfield [29] and Blossey [30], not only demonstrated the anisotropy of the III-V quantum well electronic structure but also achieved a high level of agreement between theory and experiment [31], which led to measurements of the radius, binding energy, effective mass, and the coherence length of Bloch states of the exciton [32]. However, in comparison with III-V quantum wells, thus far, EA studies on 2D MHPs have been sparse and contradictory in their analysis method as well as their assignment of features within the EA spectrum [22,23,33–35].

This study seeks to bridge the gap between the EA features of 2D MHPs and our understanding of them by simulating the EA response according to the same theory that was successful for III-V quantum wells, namely, that of a 2D Wannier exciton in a uniform field [29,36], but in a regime that accurately represents 2D MHPs (i.e., low field and low broadening). We find that this theoretical description of the EA response for 2D MHPs allows for a deeper understanding of the redshift of the exciton energy, according to the quadratic Stark effect, as well as the continuum wave function leaking into the forbidden gap, according to the Franz-Keldysh effect. Our simulated EA spectrum matches closely with our experimental measurement, and we find that all the discrepancies between the simulation and measurement can be understood in the context of charge-lattice interactions, which are not accounted for in the 2D Wannier exciton Hamiltonian. The line shape and field dependence of the measured EA response allow for direct measurements (using one fitting parameter) of the radius, polarizability, transition dipole

moment, and reduced effective mass of the exciton. In particular, the 2% uncertainty in our model-independent measurement of  $E_B$  opens the door for future studies to precisely track chemical and environmental effects on  $E_B$  and thereby add another degree of tunability to the engineering of efficient solar and light-emitting MHP devices.

## II. RESULTS AND DISCUSSION

### A. Sample preparation

Pinhole-free 2D MHP thin films with grains of about 25  $\mu\text{m}$  and a thickness of 80–120 nm are created by spin-coating a precursor solution containing a 2:1 ratio of phenethylammonium iodide (PEAI) and lead iodide ( $\text{PbI}_2$ ) to form  $\text{PEA}_2\text{PbI}_4$  on a substrate of interdigitated electrode fingers (see the Methods section for fabrication details). The small spacing between opposing electrodes (45  $\mu\text{m}$ ) allows for the generation of high applied fields (11–155 kV/cm) with moderate voltages (50–700 V) parallel to the substrate. As shown in Fig. 1(a), the  $\text{PEA}_2\text{PbI}_4$  crystal consists of alternating organic-inorganic nanolayers and thus is classified as a naturally forming quantum well material [37]. Given the high degree of anisotropy in the electronic structure of quantum wells, EA responses for 2D MHPs differ substantially when the applied field is parallel versus perpendicular to the quantum well layers [38]. To determine the quantum well orientation, we collect grazing-incidence wide-angle x-ray scattering (GIWAXS) patterns for  $\text{PEA}_2\text{PbI}_4$  films. The GIWAXS pattern in Fig. 1(b) shows  $c$ -axis diffraction peaks corresponding to the (00 $l$ ) family of crystallographic planes, confirming that the 2D layers in  $\text{PEA}_2\text{PbI}_4$  are predominately stacked with the  $c$  axis normal to the substrate [39]. To quantify the homogeneity of the grain orientations, we calculate the mosaicity factor (MF) of the off- $c$ -axis diffraction of the (002) peak. The MF value falls on a linear scale from  $-1$  to 1, corresponding to homogeneous grain orientation perpendicular ( $-1$ ) and parallel (1) to the substrate [40]. The  $\text{PEA}_2\text{PbI}_4$  thin film's MF value is 0.964, and therefore, we assume an ideal parallel case in our analysis of the EA response.

### B. Simulation of a 2D Wannier exciton in an electric field

In 2D MHPs, confinement occurs perpendicular to the quantum wells, and therefore, the in-plane EA response probed in this study is free of the quantum-confined Stark effect and quantum-confined Franz-Keldysh effect. Instead, excitons below the band gap respond to external fields via the quadratic Stark effect, while continuum states at the band gap respond via the Franz-Keldysh effect [25]. The influence of these two effects on the EA response can be precisely accounted for using the theory of Dow

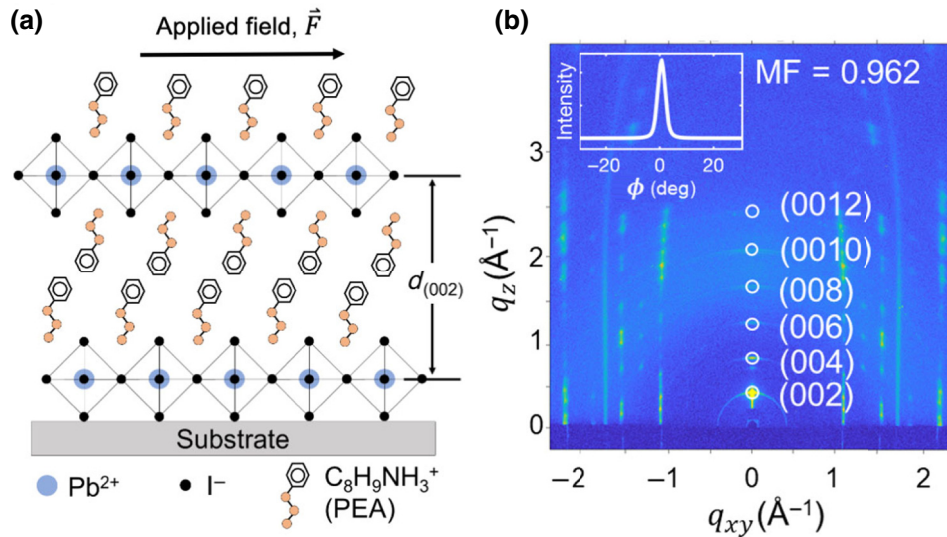


FIG. 1. (a) 2D MHP crystal structure based on a phenethylammonium lead iodide with general formula  $A_2BX_4$ , where in this case  $A$  = phenethylammonium (PEA<sup>+</sup>),  $B$  = lead (Pb<sup>2+</sup>), and  $X$  = iodide (I<sup>-</sup>). (b) GIWAXS pattern showing  $c$ -axis diffraction peaks corresponding to the  $(00l)$  family of crystallographic planes. Converting these peaks to real space via Bragg's law, we find the  $d_{002}$  spacing to be  $(1.629 \pm 0.003)$  nm. The inset shows a  $\phi$  cut of the  $(002)$  diffraction peak, which is used to calculate a mosaicity factor of 0.962, indicating the quantum wells are preferentially oriented parallel to the substrate.

and Lederman for a 2D Wannier exciton in a uniform electric field [36], based on three input parameters specific to the material: (1) the exciton's spectral linewidth,  $\Gamma$  (also known as the material's homogenous line broadening); (2) the reduced effective mass of the exciton,  $m^*$ ; and (3) the material's effective dielectric value,  $\epsilon_{r,\text{eff}}$ . For MHPs with highly frequency-dependent dielectric properties, the dielectric value of relevance here likely falls in the infrared range ( $\sim 10^{13}$  Hz) [41] and is denoted as an effective dielectric value,  $\epsilon_{r,\text{eff}}$ , which is measured by inputting the binding energy and mass into the Bohr model description of exciton binding energy [41,42].

The homogenous line broadening,  $\Gamma = 11$  meV, is found by fitting a Gaussian profile to the exciton absorption peak, as shown in Fig. 2. At first glance, there are several notable discrepancies between the absorption spectrum of PEA<sub>2</sub>PbI<sub>4</sub> [black line in Fig. 2(a)] and that of an ideal 2D Wannier exciton (red line). First, the exciton absorption for PEA<sub>2</sub>PbI<sub>4</sub> exhibits three peaks with  $(35 \pm 5)$  meV spacing, as shown in Fig. 2(b), which have been extensively studied [10,43] and recently have been shown to originate from excitonic coupling to distinct, coherent phonon modes within the [PbI<sub>6</sub>]<sup>4-</sup> layer [8,9]. Second, the 2s exciton absorption (small peak near 2.57 eV) is not

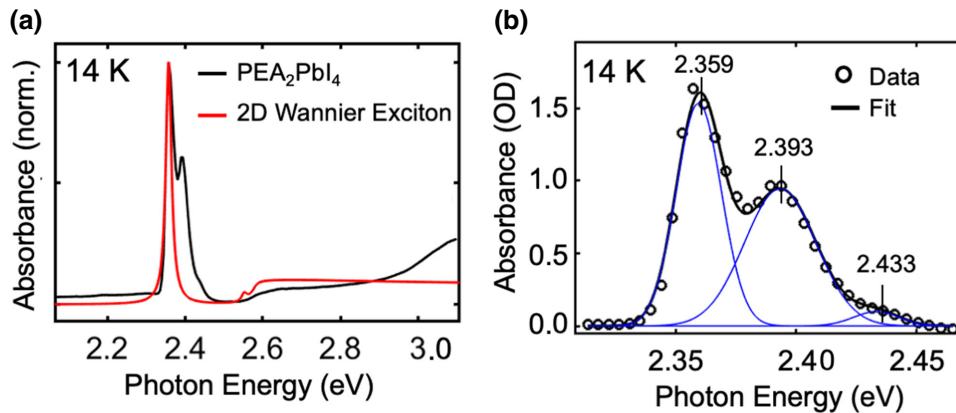


FIG. 2. (a) Absorption spectrum (black) of a PEA<sub>2</sub>PbI<sub>4</sub> thin film compared to that of a 2D Wannier exciton (red). (b) Three Gaussian profiles fit to the 1s state of the primary exciton-polaron absorption peak and two additional exciton-polaron states at higher energies. Optical phonons couple with the electrons to create the coexistence of multiple exciton-polarons with distinct lattice coupling. Half width at half maximum of the peak at 2.359 eV is measured to be 11 meV and is taken as the material's homogeneous line broadening,  $\Gamma$ .

resolved for  $\text{PEA}_2\text{PbI}_4$ , which is a result of the image charge effect suppressing the oscillator strength of the  $2s$  state, an effect that is unique in 2D MHPs [6]. Lastly, at above-gap energies,  $\text{PEA}_2\text{PbI}_4$  and other 2D MHPs exhibit multiple absorption peaks that likely arise from an overlap of the exciton continuum of states with secondary conduction-band minima. The band structure calculations of which consistently predict to be present in 2D MHPs [18,44].

Having obtained  $\Gamma$ , the EA spectrum can be simulated using reasonable estimates for  $m^*$  and  $\epsilon_{r,\text{eff}}$  in 2D MHPs. These material parameters enter the theory through the so-called ionization field ( $F_I$ ), or the field strength required to create a potential drop of one Rydberg ( $R$ ) of energy across the exciton Bohr radius ( $a_0$ ):

$$F_I = R/ea_0, \quad (2)$$

where the Rydberg energy and Bohr radius have their standard definitions:

$$R = \frac{\hbar^2}{2a_0^2 m^*}, \quad (3)$$

$$a_0 = \frac{4\pi \hbar^2 \epsilon_0 \epsilon_{r,\text{eff}}}{e^2 m^*}. \quad (4)$$

And it is the ratio between the field strength,  $F$ , and the ionization field,  $F_I$ ,

$$f = F/F_I, \quad (5)$$

that ultimately determines if the EA spectrum should be simulated in the high-field regime ( $f > 1$ ), where exciton states are ionized, or in the low-field regime ( $f < 1$ ), where ionization effects are negligible. The field strengths,  $F$ , in this study range from 2.5 to 34.5 kV/cm [45], while we estimate that the ionization field for 2D MHPs fall in the range of  $10^2$ – $10^4$  kV/cm, assuming reasonable values for  $\epsilon_{r,\text{eff}}$  between 3 and 5 and a reduced effective mass,  $m^*$ , between 0.050 and 0.221  $m_0$  [7,18]. Therefore, taking  $F < F_I$ , we simulate the EA spectrum using the theory of Ref. [36] for an ideal 2D Wannier exciton in the low-field and low-broadening regime ( $f < 1$ ,  $\Gamma \ll R$ ). We find a surprisingly high level of qualitative agreement between the measured EA response for  $\text{PEA}_2\text{PbI}_4$  [Fig. 3(a)] and that of an ideal 2D Wannier exciton in a uniform field [Fig. 3(b)]. The numerical simulation of the 2D Wannier exciton is not done to predict the band gap from first principles, but rather to elucidate the origin of previously mysterious EA features. The simulated EA of the 2D Wannier exciton is produced without any fitting parameters, only the above-stated input parameters determine the field-strength to broadening magnitudes relative to the Rydberg energy. For details on the numerical simulation, see the Numerical simulation section.

### C. $E_G$ and $E_{1s}$ assignments

As displayed in Figs. 3(a) and 3(b), the two primary features of the simulated and measured EA response for  $\text{PEA}_2\text{PbI}_4$  are (1) a first-derivative feature due to the Stark shift of the exciton energy [labeled a–c in Fig. 3(aa)], and

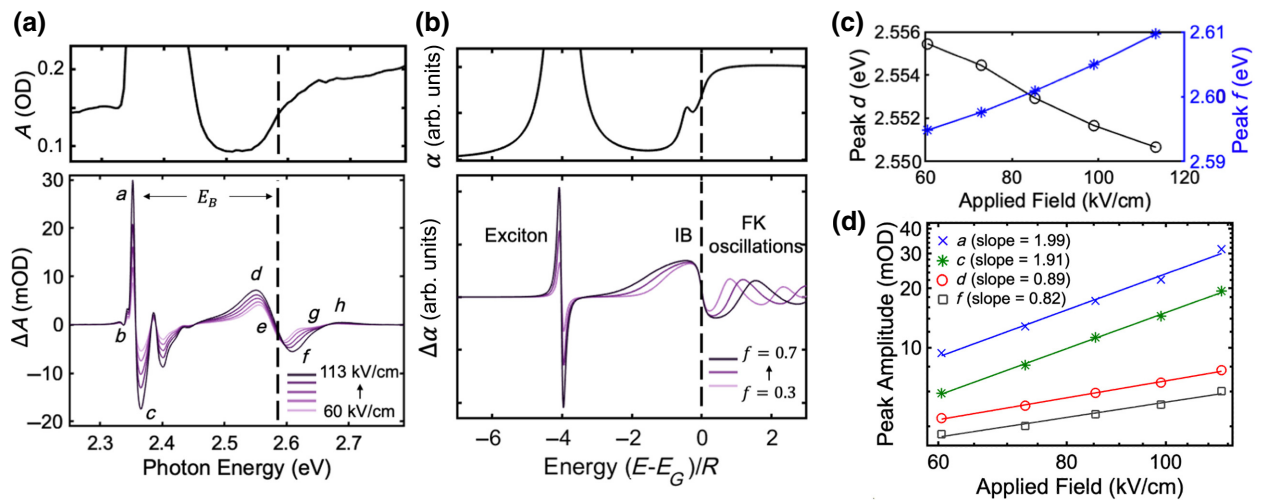


FIG. 3. (a) Absorption (top) and EA (bottom) spectra for  $\text{PEA}_2\text{PbI}_4$  at 14 K in comparison with (b) simulated absorption (top) and EA (bottom) spectra for a 2D Wannier exciton in the low-field, low-broadening regime. (c) Energy of peaks “d” and “f” as a function of applied field. Position of d decreases in energy with increasing applied field, while position of f increases as the continuum wave function leaks further into the forbidden gap. (d) Peak amplitudes as a function of applied field. Slope on the log-log scale reveals that exciton peaks “a” and “c” scale quadratically with applied field in comparison to the IB Franz-Keldysh peaks d and f, which scale sublinearly.

(2) a single oscillatory period at the interband (IB) absorption (labeled d–h). These features have been resolved in previous EA studies on 2D MHPs and, while the exciton feature clearly originates from the Stark effect, the high-energy IB feature has received contradictory interpretations, leading to miscalculations of  $E_G$  and  $E_B$  [22,23,33–35]. We find that the established theory of a 2D Wannier exciton in a uniform field [36] predicts the IB feature, as shown in the simulated spectrum in Fig. 3(b), where the horizontal axis is in energy-per-Rydberg energy ( $E_G = 0R$  and  $E_{1s} = -4R$  due to the 2D nature of the exciton). The high degree of qualitative agreement between theory and experiment demonstrates the Wannier nature of excitons in 2D MHPs. The energetic position of the IB feature at exactly  $0R$  reveals that its origin lies in the continuum wave function leaking into the forbidden gap (discussed further in the Franz-Keldysh effect section), as opposed to ionization of the  $2s$  exciton, as previously assigned [6,33,34,38]. Furthermore, the field dependence of the simulated IB feature is precisely matched in the measured EA response of  $\text{PEA}_2\text{PbI}_4$ . With increasing field strength, the wave function of  $\text{PEA}_2\text{PbI}_4$  is expected to (and does) leak further into the gap. This field dependence is plotted in Fig. 3(c), where peak d redshifts with increasing field and peak f blueshifts, indicating increased transfer of the oscillator strength from above the gap to below the gap. The crossover point, where the change in the oscillator strength switches from positive to negative (zero crossing, labeled “e”), is taken as a high-confidence measurement of the one-electron band gap energy of  $E_G = (2.579 \pm 0.004)$  eV for  $\text{PEA}_2\text{PbI}_4$ .

The assignments of the Stark and IB features are further corroborated by the field dependence of the  $\text{PEA}_2\text{PbI}_4$  EA amplitudes. We plot the amplitude of exciton peaks (a and c) and IB peaks (d and f) as a function of applied field in Fig. 3(d) and find that exciton features a and c scale with  $F^2$ , which is expected for third-order [ $\chi^{(3)}$ ] nonlinear optical processes, such as the Stark effect [46]. Meanwhile, the Franz-Keldysh effect is only a  $\chi^{(3)}$  response when the field perturbation on the continuum states is small compared with the homogenous broadening,  $\Gamma$  [47]. We observe that the field-perturbation is not small for  $\text{PEA}_2\text{PbI}_4$ , as evidenced by the fact the IB features scale linearly with  $F$ . The redshift of the exciton peak due to the quadratic Stark effect results in a sharp first-derivative EA line shape with zero crossing at point “b” marking the  $1s$  exciton resonant energy of  $E_{1s} = 2.357 \pm 0.002$  eV. The exciton binding energy,  $E_B = E_G - E_{1s}$ , is then found to be  $(222 \pm 4)$  meV, where uncertainty primarily arises from the slight variation in zero-crossing points for each field strength. Despite the fact that our simulations are founded in the hydrogenic model, we emphasize that this measurement of  $E_B$  is model independent since the Stark shift and wave function leaking phenomenon occur at critical points  $E_{1s}$  and  $E_G$  in the  $\text{PEA}_2\text{PbI}_4$  density of states. Our measurement of

$E_B = 222$  meV falls within the range of previous reports, slightly greater than the electroabsorption measurement of 190 meV reported by Zhai *et al.* [22] and slightly lower than the high-field magnetoabsorption measurements made by Dyksik *et al.* of 260 [20] and 265 meV [21]. By comparing our measured values of  $E_{1s}$  and  $E_G$  to previous reports of absorption on single crystals, one may conclude that these values not affected by the thin-film morphology. For example, Hong *et al.* correctly assigned the step edge in the absorption of single-crystal  $\text{PEA}_2\text{PbI}_4$  to the band gap at 2.58 eV and reported  $E_B = 220$  meV, in excellent agreement with our measurement on thin films [7].

Repeating this EA experiment, we find that the variation of  $E_B$  for different samples is also low. Three  $\text{PEA}_2\text{PbI}_4$  thin films and two  $\text{BA}_2\text{PbI}_4$  thin films are tested with slightly different thicknesses and processing conditions, yielding  $E_B$  values of  $(222 \pm 4)$ ,  $(222 \pm 6)$ , and  $(225 \pm 5)$  meV for  $\text{PEA}_2\text{PbI}_4$  and  $(251 \pm 2)$  and  $(248 \pm 8)$  meV for  $\text{BA}_2\text{PbI}_4$  (average values are provided in Table I). We choose to study  $\text{BA}_2\text{PbI}_4$  because, similar to  $\text{PEA}_2\text{PbI}_4$ , it is among the most commonly studied 2D MHP systems. However, unlike  $\text{PEA}_2\text{PbI}_4$  (and similar to nearly all other 2D MHP compositions), its absorption spectrum lacks a steplike feature at the band gap [48,49]. Despite lacking this feature in the absorption spectrum, we find that the IB feature is present in the EA spectra for  $\text{BA}_2\text{PbI}_4$  (see Appendix A), demonstrating that our measurement method for  $E_B$  is robust and likely can be applied to any MHP system with sufficient separation between exciton and continuum states ( $E_B \gg \Gamma$ ). We find the difference in organic cation (PEA vs BA) has essentially no effect on the EA signal: the two primary features, exciton and IB, are robustly observed with the same field dependence across all tested thin films. This result is expected given that previous studies have established the organic cation primarily affects only the electronic states by modulating the dielectric environment [48,50]. The full dataset of EA spectra and measurements of  $E_{1s}$ ,  $E_G$ , and  $E_B$  are provided in Appendix A.

Moving to higher temperatures, the broadening,  $\Gamma$ , increases and this measurement of  $E_B$  becomes less precise, as shown in Fig. 4 for  $\text{PEA}_2\text{PbI}_4$ . The  $E_{1s}$  and  $E_G$  levels blueshift with increasing temperature, consistent with the unique anti-Varshni effect expected for MHP systems [51], while  $E_B$  remains relatively constant. The uncertainty

TABLE I. Exciton binding energies averaged from multiple thin films.

	$E_B$ (meV)
$\text{PEA}_2\text{PbI}_4$ (<45 K)	$223 \pm 3$
$\text{PEA}_2\text{PbI}_4$ (300 K)	$222 \pm 10$
$\text{BA}_2\text{PbI}_4$ (<45 K)	$250 \pm 4$
$\text{BA}_2\text{PbI}_4$ (300 K)	$205 \pm 7$

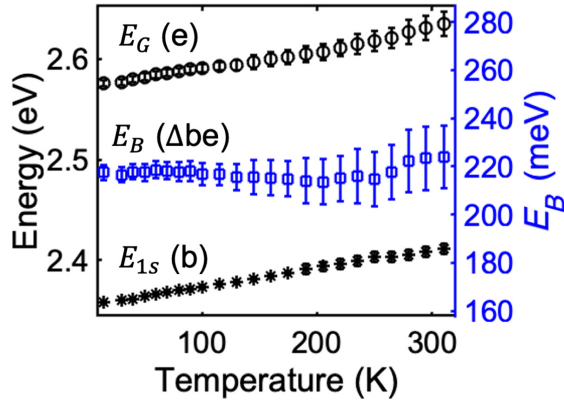


FIG. 4. Energetic positions of  $E_G$  given by zero-crossing e,  $E_{1s}$  given by zero-crossing b, and  $E_B$  given by the difference between  $E_G - E_{1s}$ . Uncertainty in  $E_{1s}$  remains low compared with the uncertainty in  $E_G$ , which increases with temperature given the decrease in the amplitude of the IB feature.

in both  $E_G$  and  $E_B$ , however, rises monotonically with temperature as zero-crossing point e become a less trustworthy as a marker for  $E_G$  due to greater homogenous and inhomogeneous broadening mechanisms. It should also be noted that, for all samples, we observe the exciton's EA line-shape transition from first derivative to second derivative with increasing temperature, as detailed in Appendix B. Therefore, for  $T \gtrsim 150$  K, zero-crossing point b can no longer be taken as  $E_{1s}$ . Rather,  $E_{1s}$  is more accurately measured by the resonance peak in the absorption spectrum with an uncertainty determined by the peak's intrinsic broadening. The high- and low-temperature values of  $E_B$  for  $\text{PEA}_2\text{PbI}_4$  and  $\text{BA}_2\text{PbI}_4$  are summarized in Table I.

#### D. Discrepancies between theory and experiment

The most noticeable discrepancy between the simulated and measured spectra lies in the additional oscillation near 2.4 eV in the  $\text{PEA}_2\text{PbI}_4$  spectrum. By plotting the EA alongside the first derivative of the absorption spectrum (Fig. 5), it is evident that the two spectra have nearly identical line shapes across the entire exciton range of 2.32–2.44 eV, indicating that all the exciton-polaron absorption peaks are uniformly redshifted by the applied field [22,52]. Thus, we assign this additional oscillation to the quadratic Stark shift of the secondary exciton-polaron state at 2.393 eV. Another notable discrepancy is that sinusoidal-like oscillations at high energies are present in the simulated EA spectrum, but not the measured spectrum. These are Franz-Keldysh oscillations and can persist over a wide spectral range in high-quality GaAs-based multiple quantum wells [32] but are not expected when conduction-band Bloch states have a short coherence length. The absence here demonstrates the magnitude of phase-disrupting perturbations in the charge carrier's energy landscape and/or the frequency of carrier-lattice

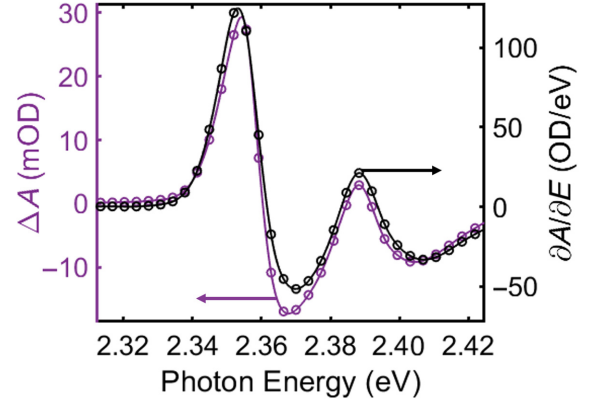


FIG. 5. EA spectrum (purple) in comparison to the first derivative of the absorption spectrum (black) in the exciton region for  $\text{PEA}_2\text{PbI}_4$ . Oscillation at 2.39 eV is caused by a Stark shift of the phonon sideband.

scattering events, which are expected for the highly disordered, highly ionic  $\text{PEA}_2\text{PbI}_4$  MHP lattice [53,54]. Thus, we find that the discrepancies in theory and experiment are consistent with charge-lattice effects, which are well documented for 2D MHPs, but that are not accounted for in the Hamiltonian of the 2D Wannier exciton. Meanwhile, the two main EA features, those being the exciton and the IB features, are well captured in the simulation. Having obtained a high-confidence measurement of  $E_B$ , we can proceed to analyze the field dependency of these features according to Stark and Franz-Keldysh theories.

#### E. Stark shift of 1s exciton

Unlike exciton states in III-V quantum wells, the large energetic separation between  $E_{1s}$  and continuum states places the excitons in 2D MHPs within a regime where ionization effects are negligible and where a perturbative approach to analyzing the exciton Stark shift is well justified. Thus, the magnitude of the linear Stark shift ( $\Delta E_L$ ) and quadratic Stark shift ( $\Delta E_Q$ ) of the 1s exciton of  $\text{PEA}_2\text{PbI}_4$  can be independently measured by fitting the EA response to first and second derivatives of the unperturbed absorbance [55] as follows:

$$\Delta A = \frac{\partial A}{\partial E} \Delta E_Q + \frac{1}{2} \frac{\partial^2 A}{\partial E^2} (\Delta E_L)^2. \quad (6)$$

Figure 6 shows the measured  $\Delta E_Q$  for two  $\text{PEA}_2\text{PbI}_4$  samples, along with the theoretical values predicted for two- and three-dimensional Wannier excitons, as given by Eqs. (7) and (8) [36,56]:

$$\frac{\Delta E_{Q,3D}}{E_B} = -\frac{9}{8} \left( \frac{ea_0 F}{E_B} \right)^2, \quad (7)$$

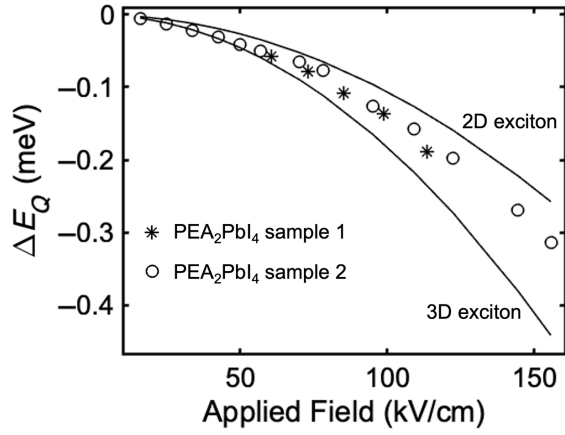


FIG. 6. In-plane quadratic Stark shift of the  $1s$  exciton for  $\text{PEA}_2\text{PbI}_4$ , compared to limits expected for 2D and 3D Wannier excitons with a Bohr radius of 2.2 nm, set by Eqs. (7) and (8), respectively.

$$\frac{\Delta E_{Q,2D}}{E_B} = -\frac{21}{32} \left( \frac{ea_0F}{E_B} \right)^2. \quad (8)$$

Here,  $E_B$  is the measured binding energy (223 meV);  $a_0$  is the 3D exciton Bohr radius, as defined in Eq. (4); and  $F$  is the field strength, i.e., the applied field screened by the dielectric value at the frequency of the modulating voltage,  $\epsilon_r$  (983 Hz). We measure this dielectric value to be 4.5 (see Appendix C). The smaller Stark shift in the 2D limit is due to the symmetry of the charge distribution in two dimensions reducing the exciton's polarizability [57,58]. The relation in Eq. (6) holds when field ionization is negligible, while Eqs. (7) and (8) are valid so long as  $\Delta E$  is small compared with  $R$ . Both requirements are well satisfied for 2D MHPs at our experimental field strengths, and therefore, we use  $\Delta E_Q$  to determine the exciton Bohr radius. Requiring the Stark shift to fall between the 3D and 2D limits, we adjust the single fitting parameter  $a_0$  in Eqs. (7) and (8) to find a lower bound of 1.9 nm and an upper bound of 2.5 nm for  $\text{PEA}_2\text{PbI}_4$  (shown in Fig. 6 for  $a_0 = 2.2$  nm). In its initial state, the exciton's true radius likely falls between the 3D Bohr radius ( $a_0 = 2.2$  nm) and 2D Bohr radius ( $a_0/2 = 1.1$  nm) limits meaning it is delocalized over a length of about 2–4  $[\text{PbI}_6]^{4-}$  octahedra parallel to the quantum well layer. However, more detailed theoretical models of MHPs must be developed to determine how subsequent polaron formation affects the radius on longer timescales [9]. Although this is the first experimental measurement of  $a_0$  in 2D MHPs that we are aware of, our window of 1.1–2.2 nm for the exciton's radius captures the rms wave function extension, measured by Dyksik *et al.* as  $\sqrt{r^2} = 1.3$  nm for  $\text{PEA}_2\text{PbI}_4$  [21].

For each field strength, the magnitude of the measured  $\Delta E_L$  and  $\Delta E_Q$  values can be straightforwardly converted

TABLE II. Exciton properties for  $\text{PEA}_2\text{PbI}_4$  at 15 K.

	$\text{PEA}_2\text{PbI}_4$
$a_0$ (nm)	$2.2 \pm 0.55$
$\mu_{ge}$ (D)	$13 \pm 4$
$\alpha_{ge}$ ( $\text{\AA}^3$ )	$80\,000 \pm 10\,300$
$m^*$ ( $m_0$ )	$0.09 \pm 0.024$

into the exciton's transition dipole moment,  $\mu_{ge}$ , and polarizability,  $\alpha_{ge}$ , according to the definitions of the quadratic and linear Stark effects [52]:

$$\Delta E_L = -\mu_{ge}F, \quad (9)$$

$$\Delta E_Q = -\frac{1}{2}\alpha_{ge}F^2, \quad (10)$$

where  $\mu_{ge}$  is the change in permanent dipole moment, and  $\alpha_{ge}$  is the change in polarizability upon a transition from the ground state to the excited state  $g \rightarrow e$ . We find our measurement of  $\mu_{ge} = (13 \pm 4)\text{D}$  for our  $\text{PEA}_2\text{PbI}_4$  thin film to be in close agreement with the value of 11 D measured in a recent optical Stark effect study by Proppe *et al.* [59]. The magnitude of the quadratic Stark shift yields a large polarizability of  $(80\,000 \pm 10\,300)\text{\AA}^3$  expected for a delocalized Wannier exciton. This polarizability value is about 10 times greater than excitons in molecular matrices [52] and 3 times greater than in inorganic quantum dots [60]. A summary of these measurements is provided in Table II.

## F. Franz Keldysh effect

The physical origin of the IB feature is rendered clear in Fig. 7(a) by comparing the zero-field band-edge absorption strength,  $\alpha(E, f=0)$ , to that of the field-shifted spectra,  $\alpha(E, f>0)$ . The maximum d and minimum f, which are large in the EA response observed for all 2D MHPs, even at room temperature, arise from the wave function leaking into the forbidden gap. Subsequent Franz-Keldysh oscillations at higher energies are less clear in the experimental EA spectra—only the first peak (labeled “h”) is resolved at low temperatures. However, as discussed previously, these oscillations dampen rapidly and even observed peak h is extremely small. The clearest example of it is shown in Fig. 7(b) for  $\text{BA}_2\text{PbI}_4$ .

The IB features d–f and Franz-Keldysh oscillations g–h can be intuitively understood as the difference between exciting into Bloch versus Airy conduction-band states, where the latter is the solution to an unbound electron in a uniform electric field. For a sufficiently high field and small mass, the oscillations in the EA spectrum take the form of an Airy function, the argument of which is the electron's kinetic energy scaled by the electro-optic energy,  $\hbar\theta$ ,

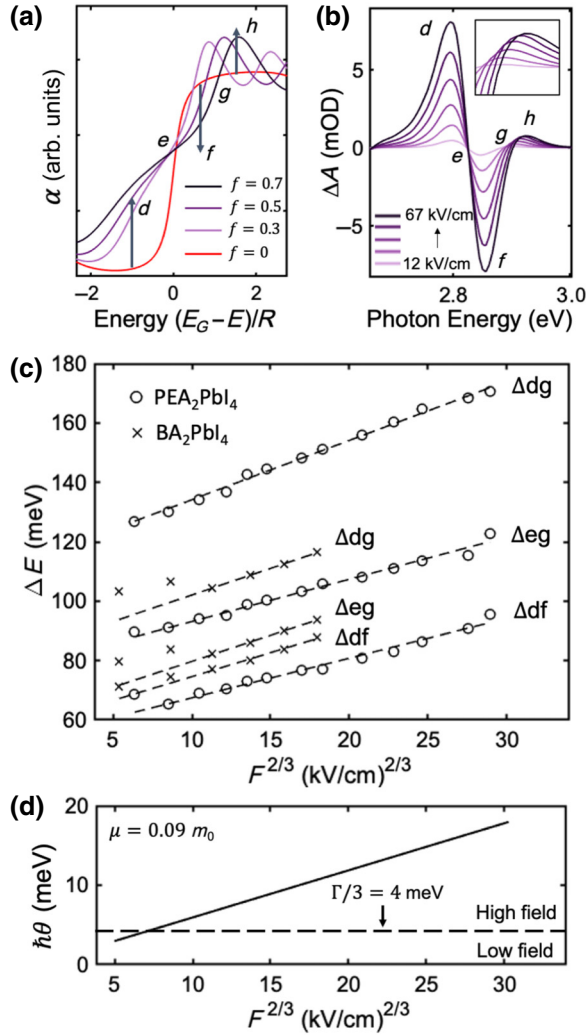


FIG. 7. (a) Band-edge absorption with increasing field simulated for a 2D Wannier exciton. (b) IB EA feature and subsequent Franz-Keldysh oscillation resolved clearly for a  $BA_2PbI_4$  sample. (c) Field broadening of the d–h EA features measured by energetic separation between critical points in the EA spectrum and plotted as a function of applied field  $F^{2/3}$ . Only data points well above the high-field Franz-Keldysh cutoff ( $F > 30$  kV/cm) are included in the fit. (d) Electro-optic energy as a function of applied field  $F^{2/3}$ . When  $\hbar\theta$  is greater than 4 meV, the EA features should be analyzed according to high-field Franz-Keldysh theory.

as follows [61,62]:

$$\text{Ai}\left(-\frac{E - E_G}{\hbar\theta}\right), \quad (11)$$

$$\hbar\theta = (\hbar^2 e^2 F^2 / 2m^*)^{1/3}, \quad (12)$$

where  $F$  is the field strength and  $m^*$  is the reduced effective mass. In the high-field regime (defined as  $\hbar\theta > \Gamma/3$ ), the amplitudes of Franz-Keldysh oscillations are

expected to scale according to  $\sqrt{\hbar\theta} \propto F^{1/3}$ , while positions should broaden according to  $\hbar\theta \propto F^{2/3}$  in accordance with the Airy function behavior [63]. Indeed, at high applied fields, we observe that spectral broadening between relative points d–h has a consistent slope proportional to  $F^{2/3}$ , as shown in Fig. 7(c). As detailed in Appendix D, we use the slope to solve for the reduced effective mass of the exciton using one fitting parameter,  $m^*$ . We find  $m^* = (0.09 \pm 0.024) m_0$  for  $PEA_2PbI_4$  and  $m^* = (0.08 \pm 0.02) m_0$  for  $BA_2PbI_4$ , where the majority of the uncertainty arises from sample-to-sample variation in the rate of field broadening. Given that the band structure for these 2D MHP compositions originate from the same  $[PbI_6]^{4-}$  octahedra layer, we expect the masses to be the same. We find that these values are consistent with measurements in 3D MHPs ( $0.12 m_0$  by Ziffer *et al.* [64] and  $0.108 m_0$  by Miyata *et al.* [17]) as well as the high-field magnetoabsorption measurement by Dyksik *et al.* of  $0.091 m_0$  [20] and  $0.087 m_0$  [21] for  $PEA_2PbI_4$  but does not agree with the low-field magnetoabsorption measurement by Blancon *et al.* of  $0.221 m_0$  for  $BA_2PbI_4$  [18].

In Fig. 7(d), we plot the resulting electro-optic energy using the mass for  $PEA_2PbI_4$  and find that the electro-optic energy surpasses the homogenous broadening ( $\Gamma/3$ ) near an applied field of 18 kV/cm [or  $6.9$  (kV/cm) $^{2/3}$ ]. Indeed, this result is concomitant with the field strength at which the field broadening in Fig. 7(c) acquires a consistent slope proportional to  $F^{2/3}$ , thus supporting the measurements of  $m^*$  and  $\Gamma$ . For lower quality samples or samples at higher temperatures, the high-field Franz-Keldysh limit will increase proportional to broadening  $\Gamma$ . The dielectric and quantum confinement effects, which enhance  $E_B$  by an order of magnitude, place 2D MHPs in a unique category where the exciton state enters the high-field regime at an ionization field of  $F_I = 944$  kV/cm [calculated according to Eq. (2)], but the continuum enters the high-field Franz-Keldysh regime at a much lower 18 kV/cm. This observation is because the high-field cutoff for the exciton depends on its radius and binding energy, while the continuum depends on the broadening and mass of the exciton.

In conclusion, we show the first observation and assignment of a continuum wave function leaking into the forbidden gap in a MHP system, according to the high-field Franz-Keldysh effect, and demonstrate that the electric field dependence of this phenomenon can be used to measure the reduced effective mass of the exciton. We additionally observe a Stark shift of the  $1s$  exciton state, which produces measurements of the radius, transition dipole moment, and polarizability of the exciton. These values place meaningful bounds on future theoretical models for 2D MHP systems. The modest in-plane radius ( $1.1$ – $2.2$  nm) and high polarizability [ $(80\,000 \pm 10\,300) \text{ \AA}^3$ ] measured herein demonstrate that exciton states in 2D MHPs are quasi-2D Wannier



excitons delocalized over 2–4  $[\text{PbI}_6]^{4-}$  octahedra parallel to the quantum wells. Despite this less-than-ideal 2D nature, the qualitative similarities between the EA response for 2D MHPs and that of an ideal 2D Wannier exciton are strong. We find the 2D MHP EA response is essentially unaffected by cation type (PEA vs BA), other than the energetic positions of the Stark and Franz-Keldysh features, and we also expect these same features to be present in the EA response of the Dion-Jacobson class of 2D MHPs. The simulation of the 2D Wannier exciton deepens our understanding of the IB feature in the EA response of 2D MHPs and leads to high-confidence, model-independent measurements of  $E_G$  and  $E_B$ . This method for measuring  $E_B$  in MHP systems opens the door for future studies to precisely track chemical and environmental effects on  $E_B$  and thereby acquire more control of this important variable in MHPs as they are assembled into functional devices for light-harvesting and light-emitting applications.

### III. METHODS

#### A. Film fabrication and characterization

We synthesize millimeter-sized  $\text{PEA}_2\text{PbI}_4$  and  $\text{BA}_2\text{PbI}_4$  single crystals by dissolving  $\text{PbO}$  (0.536 g, 2.4 mmol) and the organic amine [phenethylamine (756  $\mu\text{l}$ , 6 mmol) or butylamine (593  $\mu\text{l}$ , 6 mmol)] in excess hydroiodic acid (5 ml) stabilized with a small addition of hypophosphorous acid (75  $\mu\text{l}$ ) [65]. All chemicals are purchased from Sigma Aldrich. The solution is stirred under heat ( $\sim 70^\circ\text{C}$ ) for about 5 min until the solutes dissolve and is then removed from the hotplate, resulting in the precipitation of a bright orange solid. The crystals are then filtered with diethyl ether and dried under vacuum at  $60^\circ\text{C}$  for 2 h. The filtered and dried single crystals are brought into a glovebox ( $\sim 0.1$  ppm  $\text{O}_2$ ) and dissolved in a 4:1

mixture of dimethylformamide and dimethyl sulfoxide to target a 0.07–0.1 M solution and then stirred for 2 h at  $60^\circ\text{C}$ . We pipette the resulting precursor solution onto a  $1.2 \times 1.2$  cm<sup>2</sup> quartz substrate with interdigitated gold electrodes (Fig. 8), which is spin cast at 4500 rpm for 20 s then the film is annealed for 30 min at  $100^\circ\text{C}$ . The low molarity and high spin-casting speed produced thinner films, which is advantageous for EA both to resolve the exciton's peak at low transmission and to avoid saturating the detector at wavelengths of large transmission (peak optical density  $\approx 1$ –2). The x-ray diffraction (XRD) pattern of the EA device [shown in Fig. 8(b) for  $\text{PEA}_2\text{PbI}_4$ ] exhibits uniformly spaced diffraction peaks corresponding to the  $\{00l\}$  family of crystallographic planes. We find that the film's morphological properties are unaffected by exposure to high voltage; for example, the film's XRD pattern shows no changes after EA measurements. This observation is expected given the smooth field dependence of the EA signal, in accordance with theoretical expectations, throughout the entire range of field strengths. Previous studies have observed continuous field dependency in the EA signal of 2D perovskites for field strengths an order of magnitude greater than those in this study [6,38].

For structural characterization, GIWAXS images are acquired on beamline 11-3 at the Stanford Synchrotron Radiation Lightsource (SSRL). A 12.7-keV x-ray beam is angled at  $0.2^\circ$  with respect to the substrate, which is below the substrate's critical angle and above the film's critical angle. The diffraction pattern is collected on a  $3072 \times 3072$  pixel CCD array positioned 315 mm from the sample. All images are background, polarization, and absorption corrected using GIXSGUI software [66]. Distortion from the last two effects is negligible. The MF values are calculated according to the procedure outlined in Ref. [40]. The XRD patterns are obtained using an x-ray diffractometer (Bruker D8 Discover) with  $\text{Cu } K\alpha$  radiation (1.5406 Å).

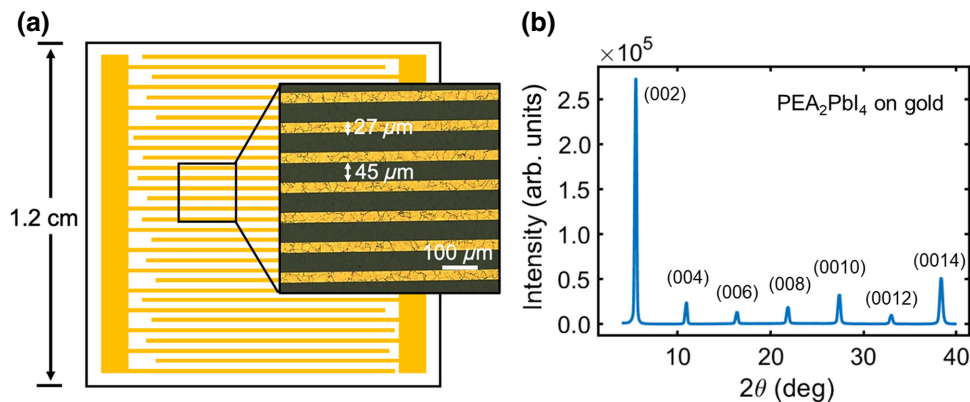


FIG. 8. (a) Substrate used for EA and dielectric spectroscopies. Gold electrodes were deposited via photolithography onto a quartz substrate with  $45 \mu\text{m}$  spacing between opposing electrodes. The inset is an optical micrograph of a  $\text{PEA}_2\text{PbI}_4$  thin film on the interdigitated fingers. (b) XRD pattern of the EA device ( $\text{PEA}_2\text{PbI}_4$  on gold electrodes) with diffraction peaks corresponding to the  $\{00l\}$  family of crystallographic planes.

## B. Electroabsorption spectroscopy

Each sample consists of a MHP thin film deposited on a photolithographically patterned array of interdigitated gold electrodes with a spacing of  $d = 45 \mu\text{m}$ , which allows for the generation of high electric fields ( $>10 \text{ kV/cm}$ ) with modest voltages ( $\sim 50\text{--}700 \text{ V}$ ), similar to those used in previous electroabsorption studies [67]. The sample is mounted in a cryostat for transmission of sample  $T$ , transmission of substrate  $T_0$ , and electrotransmission of sample  $\Delta T$ . Incandescent light from a Xe lamp is dispersed through a Digikröm 0.25 m monochromator with 1 nm spectral resolution, focused on the sample, and detected by a Thorlabs SM1PD2A photodiode detector. The rms value of the photodiode's signal is demodulated with a Stanford Research Systems SR810 lock-in amplifier operating in current mode. For  $T$  and  $T_0$ , the signal is detected at the first harmonic of the mechanical chopper's frequency (330 Hz), whereas the  $\Delta T$  signal is lock-in detected at either the first or second harmonic of the modulating signal,  $V_{\text{ac}}(t)$ , depending on which Fourier component of the squared signal,  $V_{\text{ac}}^2(t)$ , is largest. Various  $V_{\text{ac}}(t)$  waveforms are tested and found to yield consistent EA line shapes and amplitudes after instrumental correction factors are accounted for. The reported absorbance is calculated as  $A = \log_{10}(T_0/T)$ . The EA response is then given by

$$\Delta A = \log_{10}\left(\frac{T_0}{T_F}\right) - \log_{10}\left(\frac{T_0}{T}\right), \quad (13)$$

where  $T_F$  represents the field-perturbed transmission spectrum. Substituting  $T_F = \Delta T + T$ , Eq. (13) becomes

$$\Delta A = -\log_{10}\left(1 + \gamma \frac{\Delta T}{T}\right), \quad (14)$$

where an instrumental correction factor,  $\gamma$ , is introduced, which is the ratio of the rms value of the mechanical chopper signal's  $1\omega$  Fourier coefficient and the rms value of the  $V_{\text{ac}}^2(t)$  signal's  $1\omega$  (or  $2\omega$ ) Fourier coefficient [68].

## C. Numerical simulation

The numerical simulations for a 2D Wannier exciton in a uniform electric field are run on the frisco1 cluster at the Center for High Performance Computing at the University of Utah using in-house code written for Matlab R2020b. The numerical procedure we implement is based on Refs. [29,69], and we summarize it here for the two-dimensional case.

We begin with the Elliott formula for direct interband transitions, which relates a semiconductor's absorption coefficient,  $\alpha$ , to the electron-hole wave function,  $\psi_n(0)$ ,

as follows [70,71]:

$$\alpha(E) = \frac{2\pi |d_{cv}|^2 \omega}{n_b \epsilon_0 c} \sum_n |\psi_n(0)|^2 \delta(E_n - \hbar\omega), \quad (15)$$

where  $d_{cv}$  is the dipole matrix element,  $\hbar\omega$  is the photon energy,  $n_b$  is the background refractive index,  $\epsilon_0$  is the permittivity of free space, and  $c$  is the speed of light. To obtain the absorption coefficient, we must first solve for  $\psi_n(0)$ , which, in our case, corresponds to the wave function of a 2D Wannier exciton in a uniform field. In dimensionless units, this Schrödinger equation takes the following form:

$$\left(-\nabla_{x,y}^2 - \frac{2}{r} + fx\right) \psi_n(x,y) = E_n \psi_n(x,y), \quad (16)$$

where  $\psi_n(x,y)$  is the wave function for the relative motion of the electron-hole;  $E_n$  is  $\hbar\omega - E_G$ ;  $f$  is a dimensionless field defined in Eq. (5); and the label “ $n$ ” represents a quantum state with energy  $E$ , azimuthal quantum number  $m$ , and a separation parameter (or “parabolic eigenvalue”)  $t_n$ . To make Eq. (16) tractable, a transformation to parabolic coordinates is needed, as follows:

$$\xi = r + z, \quad \zeta = r - z, \quad x = \frac{1}{2}(\xi - \zeta). \quad (17)$$

A separation of variables assumption is made in parabolic coordinates, and we seek solutions of the following form:

$$\psi_n(r) = \frac{\chi_1(\xi)\chi_2(\zeta)}{(\xi\zeta)^{1/4}}. \quad (18)$$

Inserting this ansatz into Eq. (16) results in the following two quasi-Schrödinger equations:

$$\chi_1(\xi)'' + \left(\frac{1-m^2}{4\xi^2} + \frac{t_n}{\xi} + \frac{E}{4} - \frac{f\xi}{8}\right) \chi_1(\xi) = 0, \quad (19)$$

$$\chi_2(\zeta)'' + \left(\frac{1-m^2}{4\zeta^2} + \frac{1-t_n}{\zeta} + \frac{E}{4} - \frac{f\zeta}{8}\right) \chi_2(\zeta) = 0. \quad (20)$$

Here,  $t_n$  represents the separation parameter that must be numerically solved for,  $J$  is a parameter that sets the Coulomb interaction, and  $m = \pm 0.5$  corresponds to the azimuthal number for direct interband transitions in two dimensions. Thus, the problem of solving Eq. (16) is reduced to solving for  $\chi_1(\xi)$  and  $\chi_2(\zeta)$ . For given values of  $f$  and  $E$ , the numerical procedure begins by setting  $J = 1$ ,  $m = 0.5$ , and using an array of initial guesses for  $t_n$  spanning a range of approximately 0.1 to 4. The potential in Eq. (19) is positive as  $\xi \rightarrow \infty$ , and therefore, an exponentially decaying  $\chi_1$  is the first boundary condition with an asymptotic form that we determine using

the Wentzel-Kramers-Brillouin approximation. For each  $t_n$ , the Numerov method [72] is then used to integrate  $\chi_1(\xi)$  inward until its first maximum is reached. At the origin, both  $\chi_1(\xi)$  and  $\chi_2(\xi)$  can be expanded as a power series, as follows:

$$\chi_{1-UN} = \xi^{(m+1)/2} \left( 1 - \frac{t_n \xi}{m+1} + O(\xi^2) \right), \quad (21)$$

$$\chi_{2-UN} = \xi^{(m+1)/2} \left( 1 - \frac{(1-t_n)\xi}{m+1} + O(\xi^2) \right). \quad (22)$$

This power series approximation  $\chi_{1-UN}$  is similarly integrated outward from the origin until the previously determined maximum point is reached, at which point, the two halves of  $\chi_1$  are rescaled to make the amplitude continuous at the joining point. The Cooley method [73] is then implemented to compare the slopes at the joining point and determine a correction factor:

$$D = \frac{\chi'_{1,\text{out}} - \chi'_{2,\text{out}}}{\int_0^\infty [\chi(\xi)]^2 d\xi}. \quad (23)$$

This correction factor,  $D$ , is calculated for each  $t_n$  within the array and a smoothing spline is fit to the function  $D(t_n)$  to accurately determine its zero crossings. The function  $D(t_n)$  oscillates around zero with first, second, third, etc. zero-crossing nodes corresponding to  $n=1, 2, 3$ , etc. parabolic eigenvalues  $t_n$ . These values are then used as initial values of  $t_{n,i}$  and further iterative integration ( $t_{n,i+1} = t_{n,i} - D$ ) is carried out convergence is obtained [ $D < 0.02 * 2^{\text{floor}(i/10)}$ ]. This converged value of  $t_n$  is considered final and used to find  $\chi_2(\zeta)$ . We insert  $t_n$  into Eq. (22) and integrate  $\chi_{2-UN}(\zeta)$  outward from the origin according to Eq. (20). The  $\chi_2(\zeta)$  function is expected to converge to its unbound asymptotic form, which Dow and Redfield found to be [29]:

$$\chi_2(\zeta) \approx \frac{A}{(\zeta/2 + E/f)^{1/4}} \sin \left[ \frac{2}{3} f^{1/2} \left( \frac{E_n}{f} + \frac{1}{2} \zeta \right)^{3/2} + \delta \right], \quad (24)$$

where  $A$  is a normalization constant that must be solved for. At large  $\zeta$ , Eq. (23) is fit (with 0.5% accuracy) to the integrated  $\chi_{2-UN}(\zeta)$  and the normalization constant  $A$  is thereby determined. At this point, all the information necessary to calculate the field-shifted absorption coefficient,  $\alpha_F$ , has been determined. As shown in Refs. [29,71],  $\alpha_F$  depends on  $A$  and  $\chi_{1-UN}(\xi)$  as follows:

$$\alpha_F(E) \cong \alpha_0 \frac{E_G}{R} \sum_n \left( A^2 \pi^2 f^{1/2} \int_0^\infty \frac{\chi_{1-UN}^2(\xi)}{\xi} d\xi \right)^{-1}, \quad (25)$$

where  $\alpha_0$  is the 2D Wannier exciton absorption coefficient that depends on  $d_{cv}$ ,  $n_b$ , and Bohr radius  $a_0$  [71]. In our

calculations, we set the prefactor  $\alpha_0 E_G/R$  equal to one and compare only the simulated versus measured EA line shape not the amplitude. The summation in Eq. (25) is carried out for all  $n$  that contribute more than 0.1% to the total absorption coefficient, and we find typically  $n_{\text{max}} = 1, 2$ , or 3. The  $m = -0.5$  case is computed, and the two absorption coefficients are summed together. Repeating this procedure for a range of  $E$  produces the field-shifted absorption spectrum  $\alpha_F(E)$ . Analytical solutions to Eqs. (19) and (20) exist for the case of  $f = 0$ , which results in the following zero-field absorption spectrum [36]:

$$\alpha(E) \cong C \left\{ \frac{1}{\pi} \sum_n \frac{1}{[n - (1/2)]^3} \delta \left[ E + \left( n - \frac{1}{2} \right)^{-2} \right] + \frac{1}{2\pi} \frac{\Theta(E)}{1 + e^{-2\pi/\sqrt{E}}} \right\}, \quad (26)$$

where  $C$  is a normalization factor and  $\Theta(E)$  is the Heaviside step function. The  $\alpha_F(E)$  and  $\alpha(E)$  spectra are then integrated and  $C$  is adjusted to make the spectral weight equal. Next, the two spectra,  $\alpha_F(E)$  and  $\alpha(E)$ , are numerically convolved with a Lorentzian function,  $L(E)$ , with a half width at half maximum of  $\Gamma$  and subtracted to produce the simulated EA spectrum  $\Delta\alpha$ :

$$\Delta\alpha = \alpha_F(E) * L(E) - \alpha(E) * L(E). \quad (27)$$

We use an  $L(E)$  with  $\Gamma = 0.15$ , which is our measurement of the  $\text{PEA}_2\text{PbI}_4$  homogenous line broadening,  $\Gamma = 11$  meV, in units of  $R$ . We note that  $R$  can be reasonably determined multiple ways. The standard conversion for 2D systems is  $E_B = 4R$ ; however, this relationship is inexact for 2D MHPs since the excitons are not fully confined to a 2D plane and they additionally experience an  $E_B$ -enhancing image charge effect. A more accurate value for  $R$  can be determined by inputting our measurements of  $a_0$  and  $m^*$  into Eq. (3), which results in  $R = 87$  meV. If instead we use our measurement of  $m^*$  and  $\epsilon_r = 4.3$  (see Appendix D), this results in  $R = 66$  meV. We chose a value between those two, namely  $R = 73$  meV for our conversion of  $\Gamma$ .

Using our measurement of  $F_I = 944$  kV/cm, the field strengths in this study correspond to an excitonic dimensionless field ranging from 0.004 to 0.06. However, these values of  $f$  correspond to a theoretical exciton peak width from about  $10^{-1152}$  to  $10^{-74} R$ , only a slight increase from the zero-field case of a Dirac-delta function [25]. Therefore, the field-shifted absorption of 2D MHPs in the excitonic range cannot be accurately simulated, even with quadruple precision in  $E$ . However, we find that simulating in a slightly higher field range of  $0.3 < f < 0.7$ , elucidates the origin of the IB feature and, therefore, is sufficient for the purposes of this study.

The IB absorption, on the other hand, can be simulated at lower fields. We find the linear field dependence of the

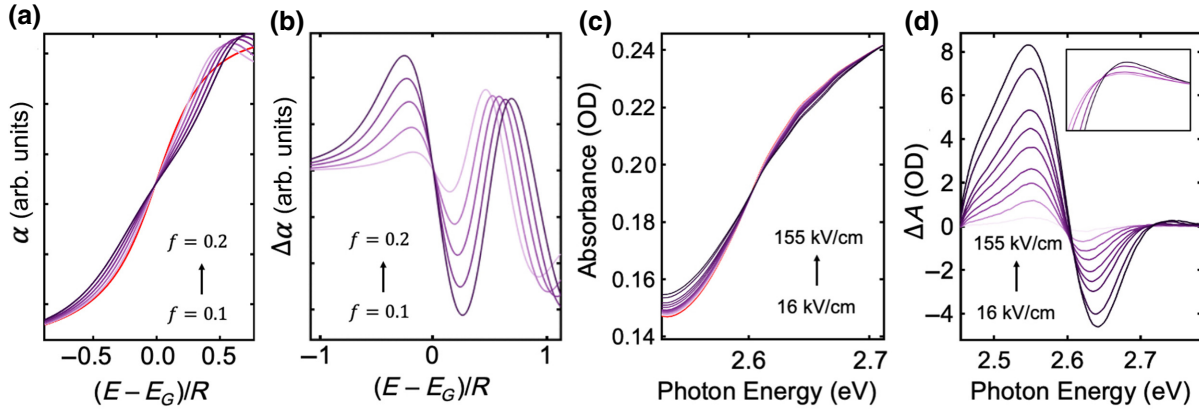


FIG. 9. (a) Simulated absorption and (b) EA in the IB range for small dimensionless fields 0.1–0.2. (c) Measured field-shifted absorption and (d) EA in the IB range for  $\text{PEA}_2\text{PbI}_4$ .

IB feature’s amplitude to be well captured by the simulation at low fields,  $0.1 < f < 0.2$ , as shown in Fig. 9. We choose this dimensionless field range, which is about 3 times larger than the exciton’s dimensionless field, since the IB absorption is purely determined by the electro-optic energy relative to the homogenous broadening and, therefore, is not affected by the  $E_B$ -enhancing image charge effect, which places the exciton in the extremely low-field range.

### ACKNOWLEDGMENTS

This work is supported by the U.S. Department of Energy, Office of Basic Energy Sciences, Division of Materials Sciences and Engineering under Award No. DE-SC0019041. K.H. would like to acknowledge support from the National Science Foundation through a Graduate Research Fellowship (Grant No. 1747505). Use of the Stanford Synchrotron Radiation Lightsource, SLAC National Accelerator Laboratory, is supported by the US DOE, Office of Science, Office of Basic Energy Sciences under Contract No. DE-AC02-76SF00515. L.W.B. would also like to acknowledge the Sloan Foundation through an Alfred P. Sloan Research Fellowship in Chemistry. We would also like to thank Dr. Thomas Pedersen, Dr. Mark Ziffer, and Dr. XiYao Zhang for helpful discussions.

### APPENDIX A: EA DATASET

In Table III, we provide the full dataset of  $E_{1s}$ ,  $E_G$ , and  $E_B$  measurements for five 2D MHP samples at low and high temperatures. The  $\text{BA}_2\text{PbI}_4$  composition undergoes a phase transition near 250 K [19,23] while  $\text{PEA}_2\text{PbI}_4$  does not. The IB feature’s zero crossing is taken as  $E_G$ , while the exciton’s zero crossing is taken as  $E_{1s}$  only for low temperatures. Above about 150 K,  $E_{1s}$  is more accurately determined as the maximum of the

exciton’s absorption peak. The sample-to-sample variation of about 20 meV in  $E_{1s}$  and  $E_G$  is likely primarily caused by differences in the sample temperature, given that the difference  $E_G - E_{1s}$  is remarkably consistent. Room-temperature EA spectrum is not measured for  $\text{PEA}_2\text{PbI}_4$  sample 2.

The field-dependent EA spectra corresponding to the measurements in Table III are displayed in Fig. 10 for  $\text{PEA}_2\text{PbI}_4$  and Fig. 11 for  $\text{BA}_2\text{PbI}_4$ . The IB feature appears larger for  $\text{BA}_2\text{PbI}_4$  samples 1 and 2 and  $\text{PEA}_2\text{PbI}_4$  sample 3 due to the smaller range of field strengths (10–70 kV/cm). As the field strength increases, the growth of the exciton’s amplitude outpaces the IB feature due to its quadratic dependence and results in proportionately smaller IB features, as is the case for  $\text{PEA}_2\text{PbI}_4$  sample 1 [Fig. 10(a)] and  $\text{PEA}_2\text{PbI}_4$  sample 2 [Fig. 10(b)], where the field strength is extended past 110 kV/cm. Due to the coexistence of high- and low-temperature crystal phases in the  $\text{BA}_2\text{PbI}_4$  samples [19,23], two exciton peaks (Stark shifts) are observed in the absorption (EA) spectrum at low temperature [Figs. 11(a) and 11(c)]. We

TABLE III.  $E_{1s}$ ,  $E_G$ , and  $E_B$  measurements of all 2D MHP samples.

	$E_{1s}$ (eV)	$E_G$ (eV)	$E_B$ (meV)
Low temperature ( $\leq 50$ K)			
$\text{PEA}_2\text{PbI}_4$ sample 1	$2.357 \pm 0.002$	$2.579 \pm 0.004$	$222 \pm 4$
$\text{PEA}_2\text{PbI}_4$ sample 2	$2.378 \pm 0.002$	$2.603 \pm 0.005$	$225 \pm 5$
$\text{PEA}_2\text{PbI}_4$ sample 3	$2.384 \pm 0.004$	$2.606 \pm 0.004$	$222 \pm 6$
$\text{BA}_2\text{PbI}_4$ sample 1	$2.551 \pm 0.0015$	$2.802 \pm 0.0015$	$251 \pm 2$
$\text{BA}_2\text{PbI}_4$ sample 2	$2.578 \pm 0.008$	$2.826 \pm 0.002$	$248 \pm 8$
High temperature ( $\sim 300$ K)			
$\text{PEA}_2\text{PbI}_4$ sample 1	$2.411 \pm 0.01$	$2.635 \pm 0.012$	$224 \pm 16$
$\text{PEA}_2\text{PbI}_4$ sample 3	$2.404 \pm 0.01$	$2.624 \pm 0.0035$	$220 \pm 11$
$\text{BA}_2\text{PbI}_4$ sample 1	$2.422 \pm 0.01$	$2.631 \pm 0.002$	$209 \pm 10$
$\text{BA}_2\text{PbI}_4$ sample 2	$2.455 \pm 0.01$	$2.656 \pm 0.003$	$201 \pm 10$

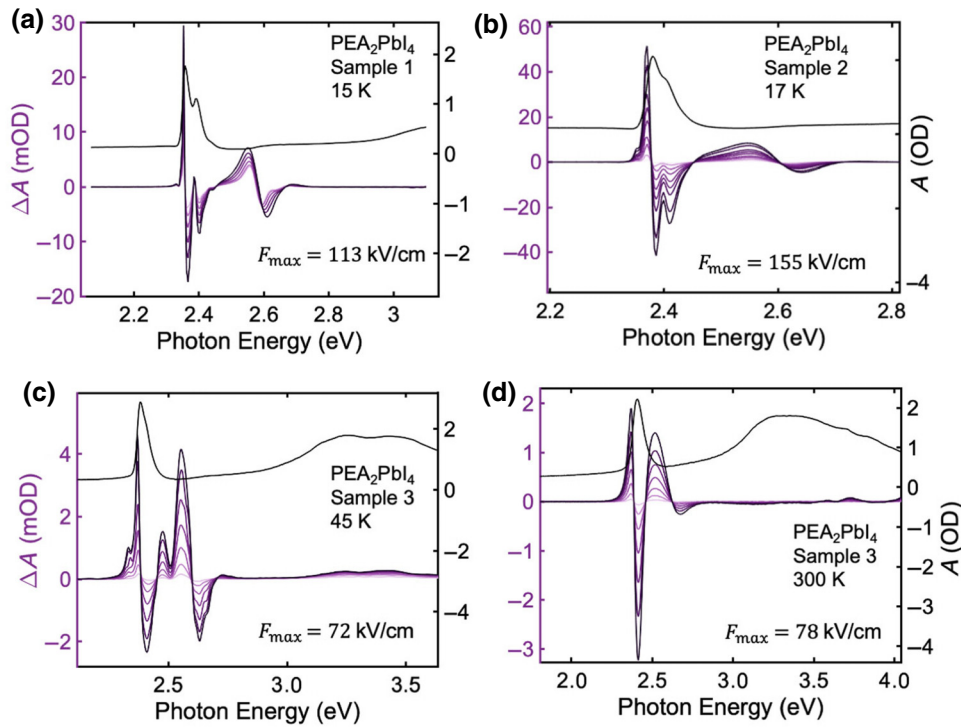


FIG. 10. Low- and high-temperature EA spectra of three  $\text{PEA}_2\text{PbI}_4$  thin films. Voltage series for the 300 K spectrum is only measured for  $\text{PEA}_2\text{PbI}_4$  sample No. 3.

note that the absorption spectra for  $\text{BA}_2\text{PbI}_4$  sample 1 in Fig. 11(a) appears to have a substantial Urbach tail, indicating poor sample morphology. However, the agreement between the EA spectrum for  $\text{BA}_2\text{PbI}_4$  sample 1 and sample 2 indicates that this difference in morphology has no effect on the EA response. Lastly, we note that, for  $\text{PEA}_2\text{PbI}_4$  sample 3,  $\text{BA}_2\text{PbI}_4$  sample 1, and  $\text{BA}_2\text{PbI}_4$  sample 2, there is a difference in lamp power between the substrate transmission and the sample transmission measurements, and therefore, the absorption spectra for these samples should be viewed as approximations. For this reason, quantitative analysis of these samples is limited to the EA spectra, which depends only on the electrotransmission and transmission of the sample. For  $\text{PEA}_2\text{PbI}_4$  sample 1, we present the temperature-dependent absorption and EA in Appendix B.

## APPENDIX B: TEMPERATURE-DEPENDENT EA

We observe that the exciton's EA line shape transitions from first to second derivative upon moving from low to high temperature for all the 2D MHPs tested in this study, as shown in Fig. 12. For this reason, the exciton's zero-crossing point in the EA spectrum is not a valid measurement of  $E_{1s}$ , for temperatures  $\gtrsim 150$  K, but rather, is more accurately determined by the free exciton absorption peak. To the best of our knowledge, a strong temperature dependence in the EA line shape has previously only been

observed for solvated dye molecules [74]. We suspect the transition is caused by an increased dipole moment, which would result in a second-derivative line shape, according to the linear Stark effect, as is clear from Eqs. (6) and (9). Disorder is shown to induce large dipole moments in molecular systems [75]. A similar effect may be present here, but with disorder arising from the thermal motion of the lattice (which is large for 2D MHPs [76,77]), rather than static morphological disorder in a molecular matrix; however, further testing of this hypothesis is beyond the scope of this study.

Absorption and EA spectra are collected at intervals of 10–15 K, moving from low temperature to room temperature, as shown in Fig. 13, for an applied field of 113 kV/cm. We measure the homogenous broadening at room temperature to be  $\Gamma = 55$  meV; thus, an applied field greater than 165 kV/cm would be needed to observe high-field Franz-Keldysh behavior ( $\hbar\theta > \Gamma/3$ ).

## APPENDIX C: MEASUREMENT OF DIELECTRIC VALUE

For the measurements of  $a_0$ ,  $\mu_{ge}$ ,  $\alpha_{ge}$ , and  $m^*$ , it is necessary to know the applied field strength experienced by the exciton, which depends on the rms amplitude of the modulating square wave,  $V_{ac}$ ; the distance between opposing interdigitated electrode fingers,  $d$ ; and the dielectric constant at the frequency of the modulating

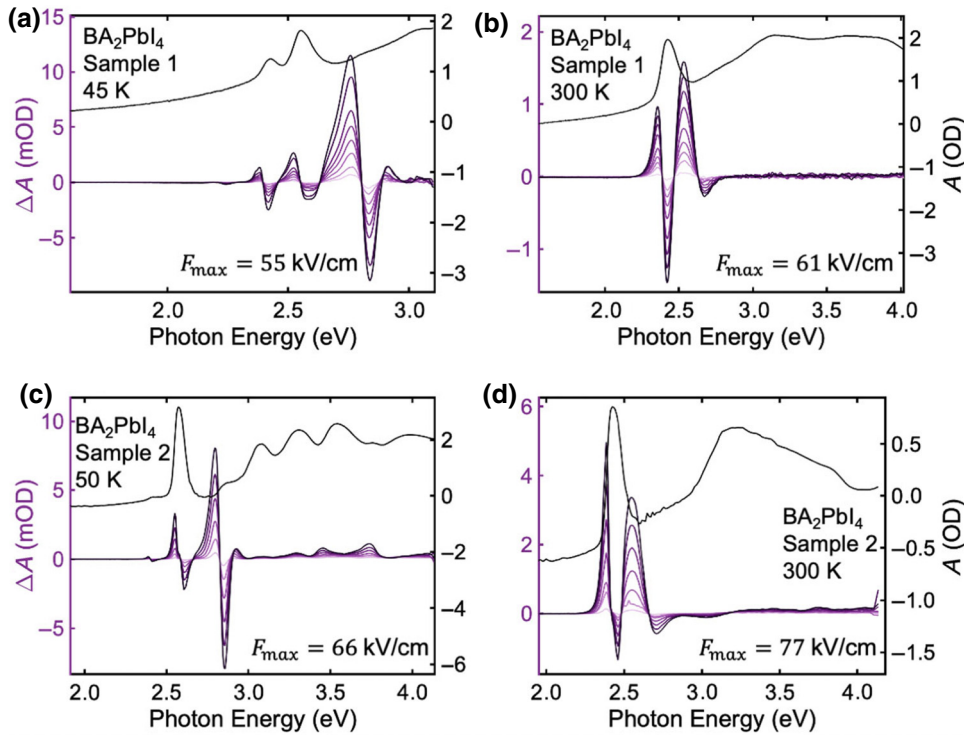


FIG. 11. Low- and high-temperature EA spectra for two  $\text{BA}_2\text{PbI}_4$  thin films. Difference between exciton and IB features is used to measure the exciton binding energy, and rate of field broadening in the Franz-Keldysh oscillation is used to measure the reduced effective mass of the exciton for  $\text{BA}_2\text{PbI}_4$ .

voltage,  $\epsilon_r(983 \text{ Hz})$ :

$$F = \frac{V_{ac}}{d \epsilon_r(983 \text{ Hz})}. \quad (C1)$$

To obtain  $\epsilon_r(983 \text{ Hz})$ , we perform dielectric spectroscopy using two geometries. First, a 1.54-mm-thick pressed pellet of  $\text{PEA}_2\text{PbI}_4$  is placed in a parallel-plate geometry

and the capacitance as a function of frequency is collected using a Hewlett Packard 4192A impedance analyzer. The capacitance values are converted into the real part of the complex permittivity according to the air-gap method in Ref. [78]. These results are plotted as circles in Fig. 14(a). Second, the capacitance of about 2- $\mu\text{m}$ -thick  $\text{PEA}_2\text{PbI}_4$  films on interdigitated fingers is measured and converted into the dielectric value according to equations

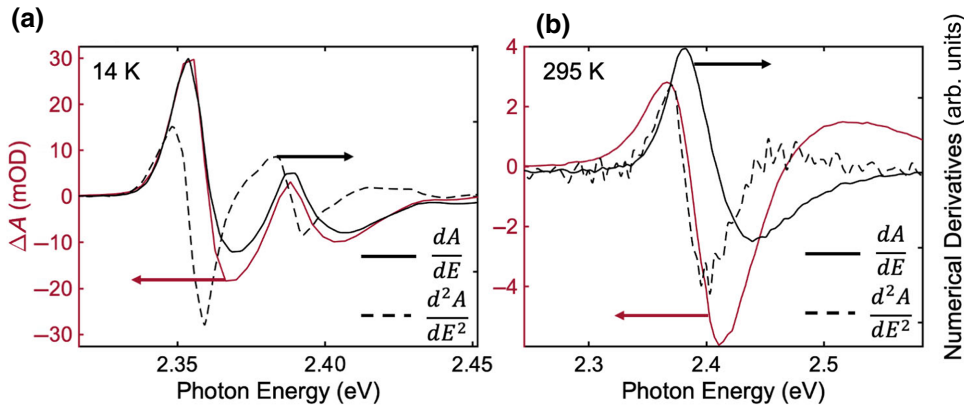


FIG. 12. (a) Low-temperature EA spectrum (red) for  $\text{PEA}_2\text{PbI}_4$  compared to first (solid black) and second (dotted black) numerical derivatives of the absorbance spectrum. The EA line shape closely matches the first derivative. For first derivative line shapes, the peak of the underlying feature is given by the position of the zero crossing. In contrast, (b) the room temperature EA spectrum more closely resembles the second derivative of the absorbance and the zero-crossing point is an inaccurate measurement of the peak position.

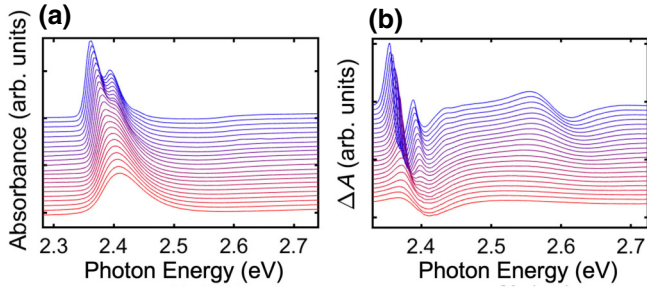


FIG. 13. (a) Absorbance and (b) EA spectra of  $\text{PEA}_2\text{PbI}_4$  sample 1 from 30 K (blue) to 310 K (red) using an applied field of 113 kV/cm.

in Ref. [79], which we modify to fit the thin-film geometry [80]. As shown in Fig. 14(a), the two methods agree at high frequencies and  $\epsilon_r$  (13 MHz) ranges from 4.1 to 4.5. However, at low frequencies, the dielectric values rise exponentially at different rates, likely caused by ion migration effects common in MHPs [81]. However, we find this exponential rise to be highly dependent on the film thickness. As shown in Fig. 14(b), the normalized capacitance between 100 and  $10^5$  Hz falls by 2 orders of magnitude for the 2.61- $\mu\text{m}$ -thick film, whereas the capacitance of the 100-nm-thick film merely decreases by a factor of 0.81. The thicknesses of the films used for EA measurements range from 80 to 100 nm. Unfortunately, however, the capacitance of the 100-nm-thick film cannot be converted into  $\epsilon_r$  because the film's thickness is comparable to the electrode thickness and, therefore, violates the model used to relate the capacitance of the interdigitated electrodes to the dielectric constant [79]. Therefore, to obtain the 983 Hz dielectric value in the 100-nm-thick film, we scale the measured high-frequency value of  $\epsilon_r(13 \text{ MHz}) = 4.3$  by the 5% capacitive increase between 13 MHz and 983 Hz observed for the 100-nm-thick film, resulting in a value of  $\epsilon_r(983 \text{ Hz}) = 4.5$ . This value agrees with estimates in the literature [7,18]. Our conclusion that ion migration effects are small in the 100-nm-thick film is corroborated by frequency-dependent EA. In about 100-nm-thick films, the exciton's EA magnitude (which scales  $\propto F^2$ ) is found to be frequency independent in the 1000–2000 Hz range but decreases slightly moving from 1000 to 500 Hz.

#### APPENDIX D: MEASUREMENT OF REDUCED EFFECTIVE MASS

In the high-field limit, Franz-Keldysh features broaden according to the argument of the Airy function in Eq. (11). Point e in the EA spectrum corresponds to zero, while the first peak, h, occurs at the Airy function's first root, 1.01 879. Thus, the spacing between zero-crossing e and the first positive peak, h, in the EA spectrum depends on

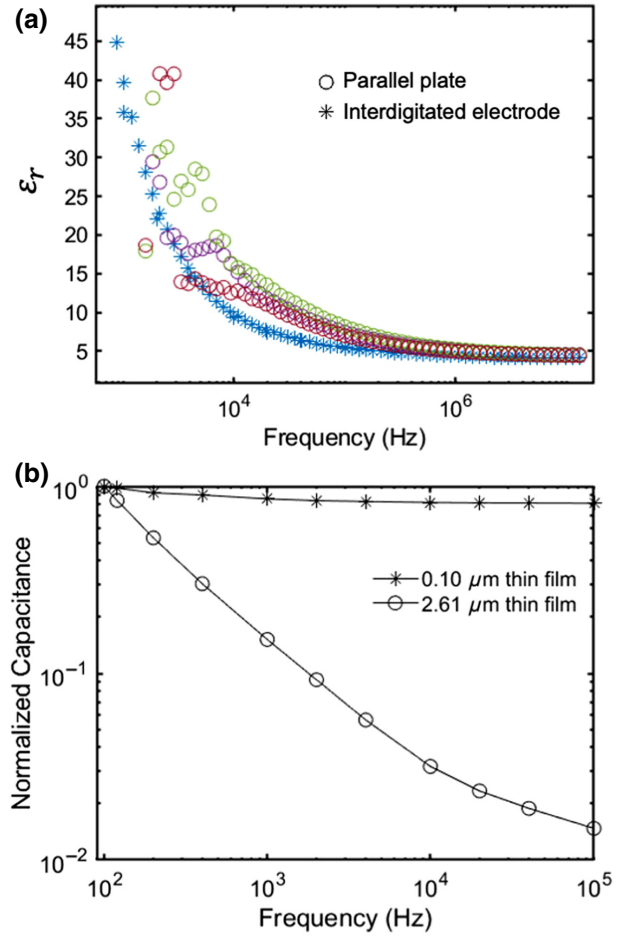


FIG. 14. (a) Real part of the  $\text{PEA}_2\text{PbI}_4$  permittivity as a function of frequency measured with various methods: a 2.61- $\mu\text{m}$ -thick film on interdigitated fingers (blue stars) and a 1.54-mm-thick pressed pellet in an air-gap parallel-plate geometry using a 1.28-mm air gap (green circles), a 1.35-mm air gap (green circles), and a 1.5-mm air gap (red circles). (b) Normalized capacitance as a function of frequency for a thin (0.10  $\mu\text{m}$ ) and thick (2.61  $\mu\text{m}$ )  $\text{PEA}_2\text{PbI}_4$  film spin cast onto interdigitated electrodes.

the electro-optic energy as follows:

$$\frac{h - E_G}{\hbar\theta} - \frac{e - E_G}{\hbar\theta} = 1.01\ 879 \quad (\text{D1})$$

TABLE IV. Dimensionless spacing between points in the Franz-Keldysh EA feature.

	Numerical factor
$\Delta eh$	1.01 879
$\Delta dh$	1.37 $\Delta eh$
$\Delta dg$	1.10 $\Delta eh$
$\Delta eg$	0.70 $\Delta eh$
$\Delta df$	0.65 $\Delta eh$

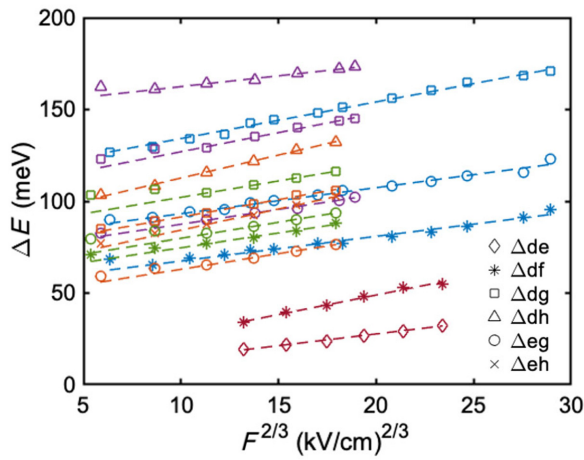


FIG. 15. Broadening of all EA features used to measure the reduced effective mass for  $\text{PEA}_2\text{PbI}_4$  and  $\text{BA}_2\text{PbI}_4$ . Different colors represent broadening of the five samples tested (maroon, blue, purple,  $\text{PEA}_2\text{PbI}_4$  samples 1, 2, 3; orange, green,  $\text{BA}_2\text{PbI}_4$  samples 1, 2). Sample-to-sample variation between common critical points is quite large. For example, the magnitude of  $\Delta dh$  (triangles) differs by 55 meV between  $\text{BA}_2\text{PbI}_4$  sample 1 and  $\text{PEA}_2\text{PbI}_4$  sample 3; however, we find the slopes to be sufficiently consistent to measure the reduced effective mass of the exciton with  $1\sigma$  variance of 27%.

Solving for  $\Delta eh$  as a function of  $F^{2/3}$  results in

$$\Delta eh = 1.01879 \left( \frac{\hbar^2 e^2}{2m^*} \right)^{1/3} F^{2/3}. \quad (\text{D2})$$

The mass is then determined from the slope of  $\Delta eh$  versus  $F^{2/3}$ . The field broadening of points other than  $\Delta eh$  can also be used to determine the mass, provided the correct numerical factor is used in place of the Airy function's first root, 1.01879. We determine these numerical factors, relative to  $\Delta eh$ , from their spacing in the simulated 2D Wannier EA spectrum. These numerical factors are given in Table IV. To calculate the mass, we include broadening between all Franz-Keldysh features, wherein the peak or zero-crossing positions are clearly resolved. The mean and standard deviation of these slopes (shown in Fig. 15) are computed to yield the mass and standard error reported in the main text.

- [1] M. A. Green, A. Ho-Baillie, and H. J. Snaith, The emergence of perovskite solar cells, *Nat. Photonics* **8**, 506 (2014).
- [2] J. M. Frost, K. T. Butler, F. Brivio, C. H. Hendon, M. van Schilfhaarde, and A. Walsh, Atomistic origins of high-performance in hybrid halide perovskite solar cells, *Nano Lett.* **14**, 2584 (2014).

- [3] Z.-K. Tan, *et al.*, Bright light-emitting diodes based on organometal halide perovskite, *Nat. Nanotechnol.* **9**, 687 (2014).
- [4] J. Even, L. Pedesseau, and C. Katan, Understanding quantum confinement of charge carriers in layered 2D hybrid perovskites, *ChemPhysChem* **15**, 3733 (2014).
- [5] C. M. Mauck and W. A. Tisdale, Excitons in 2D organic-inorganic halide perovskites, *Trends Chem.* **1**, 380 (2019).
- [6] K. Tanaka, T. Takahashi, T. Kondo, T. Umebayashi, K. Asai, and K. Ema, Image charge effect on Two-dimensional excitons in an inorganic-organic quantum-well crystal, *Phys. Rev. B* **71**, 045312 (2005).
- [7] X. Hong, T. Ishihara, and A. Nurmikko, Dielectric confinement effect on excitons in  $\text{PbI}_4$ -based layered semiconductors, *Phys. Rev. B* **45**, 6961 (1992).
- [8] F. Thouin, D. A. Valverde-Chávez, C. Quarti, D. Cortecchia, I. Bargigia, D. Beljonne, A. Petrozza, C. Silva, and A. R. Srimath Kandada, Phonon coherences reveal the polaronic character of excitons in Two-dimensional lead halide perovskites, *Nat. Mater.* **18**, 349 (2019).
- [9] A. R. Srimath Kandada and C. Silva, Exciton polarons in Two-dimensional hybrid metal-halide perovskites, *J. Phys. Chem. Lett.* **11**, 3173 (2020).
- [10] S. Neutzner, F. Thouin, D. Cortecchia, A. Petrozza, C. Silva, and A. R. Srimath Kandada, Exciton-Polaron spectral structures in Two-dimensional hybrid lead-halide perovskites, *Phys. Rev. Mater.* **2**, 064605 (2018).
- [11] J.-C. Blancon, *et al.*, Extremely efficient internal exciton dissociation through edge states in layered 2D perovskites, *Science* **355**, 1288 (2017).
- [12] J. Yin, R. Naphade, L. Gutiérrez Arzaluz, J.-L. Brédas, O. M. Bakr, and O. F. Mohammed, Modulation of broad-band emissions in Two-dimensional (100)-oriented Ruddlesden-Popper hybrid perovskites, *ACS Energy Lett.* **5**, 2149 (2020).
- [13] G. Grancini, *et al.*, One-Year stable perovskite solar cells by 2D/3D interface engineering, *Nat. Commun.* **8**, 1 (2017).
- [14] M. Yuan, *et al.*, Perovskite energy funnels for efficient light-emitting diodes, *Nat. Nanotechnol.* **11**, 872 (2016).
- [15] H. Zhang, Q. Liao, Y. Wu, Z. Zhang, Q. Gao, P. Liu, M. Li, J. Yao, and H. Fu, 2D Ruddlesden-Popper perovskites microring laser array, *Adv. Mater.* **30**, 1706186 (2018).
- [16] W. Nie, *et al.*, High-Efficiency solution-processed perovskite solar cells with millimeter-scale grains, *Science* **347**, 522 (2015).
- [17] A. Miyata, A. Mitioglu, P. Plochocka, O. Portugall, J. T.-W. Wang, S. D. Stranks, H. J. Snaith, and R. J. Nicholas, Direct measurement of the exciton binding energy and effective masses for charge carriers in organic-inorganic Tri-halide perovskites, *Nat. Phys.* **11**, 582 (2015).
- [18] J. C. Blancon, *et al.*, Scaling Law for excitons in 2D perovskite quantum wells, *Nat. Commun.* **9**, 2254 (2018).
- [19] O. Yaffe, A. Chernikov, Z. M. Norman, Y. Zhong, A. Velauthapillai, A. van der Zande, J. S. Owen, and T. F. Heinz, Excitons in ultrathin organic-inorganic perovskite crystals, *Phys. Rev. B* **92**, 045414 (2015).
- [20] M. Dyksik, *et al.*, Broad tunability of carrier effective masses in Two-dimensional halide perovskites, *ACS Energy Lett.* **5**, 3609 (2020).



- [21] M. Dyksik, S. Wang, W. Paritmongkol, D. K. Maude, W. A. Tisdale, M. Baranowski, and P. Plochocka, Tuning the excitonic properties of the 2D  $(\text{PEA})_2(\text{MA})_{n-1}\text{Pb}_n\text{I}_{3n+1}$  perovskite family via quantum confinement, *J. Phys. Chem. Lett.* **12**, 1638 (2021).
- [22] Y. Zhai, S. Baniya, C. Zhang, J. Li, P. Haney, C.-X. Sheng, E. Ehrenfreund, and Z. V. Vardeny, Giant Rashba splitting in 2D organic-inorganic halide perovskites measured by transient spectroscopies, *Sci. Adv.* **3**, e1700704 (2017).
- [23] E. Amerling, S. Baniya, E. Lafalce, C. Zhang, Z. V. Vardeny, and L. Whittaker-Brooks, Electroabsorption spectroscopy studies of  $(\text{C}_4\text{H}_9\text{NH}_3)_2\text{PbI}_4$  organic-inorganic hybrid perovskite multiple quantum wells, *J. Phys. Chem. Lett.* **8**, 4557 (2017).
- [24] D. A. B. Miller, D. S. Chemla, T. C. Damen, A. C. Gossard, W. Wiegmann, T. H. Wood, and C. A. Burrus, Band-Edge Electroabsorption in Quantum Well Structures: The Quantum-Confined Stark Effect, *Phys. Rev. Lett.* **53**, 2173 (1984).
- [25] D. A. B. Miller, D. S. Chemla, T. C. Damen, A. C. Gossard, W. Wiegmann, T. H. Wood, and C. A. Burrus, Electric field dependence of optical absorption near the band gap of quantum-well structures, *Phys. Rev. B* **32**, 1043 (1985).
- [26] G. Bastard, E. Mendez, L. Chang, and L. Esaki, Exciton binding energy in quantum wells, *Phys. Rev. B* **26**, 1974 (1982).
- [27] G. Bastard, E. Mendez, L. Chang, and L. Esaki, Variational calculations on a quantum well in an electric field, *Phys. Rev. B* **28**, 3241 (1983).
- [28] E. Mendez, F. Agullo-Rueda, and J. Hong, Stark Localization in GaAs-GaAlS Superlattices Under an Electric Field, *Phys. Rev. Lett.* **60**, 2426 (1988).
- [29] J. D. Dow and D. Redfield, Electroabsorption in semiconductors: The excitonic absorption edge, *Phys. Rev. B* **1**, 3358 (1970).
- [30] D. F. Blossey, Wannier exciton in an electric field. II. electroabsorption in direct-band-gap solids, *Phys. Rev. B* **3**, 1382 (1971).
- [31] M. Kneissl, N. Linder, P. Kiesel, S. Quassowski, K. Schmidt, G. H. Döhler, H. Grothe, and J. S. Smith, Two-Dimensional Franz-Keldysh effect in MQW structures with lateral electric fields, *Superlattices Microstruct.* **16**, 109 (1994).
- [32] A. Jaeger, G. Weiser, P. Wiedemann, I. Gyuro, and E. Zielinski, The sizes of coherent band states in semiconductors, derived from the Franz-Keldysh effect, *J. Phys.: Condens. Matter* **8**, 6779 (1996).
- [33] K. Tanaka, F. Sano, T. Takahashi, T. Kondo, R. Ito, and K. Ema, Two-Dimensional wannier excitons in a layered-perovskite-type crystal  $(\text{C}_6\text{H}_{13}\text{NH}_3)_2\text{PbI}_4$ , *Solid State Commun.* **122**, 249 (2002).
- [34] K. Tanaka and T. Kondo, Bandgap and exciton binding energies in lead-iodide-based natural quantum-well crystals, *Sci. Technol. Adv. Mater.* **4**, 599 (2003).
- [35] V. Kattoor, K. Awasthi, E. Jokar, E. W.-G. Diao, and N. Ohta, Integral method analysis of electroabsorption spectra and electrophotoluminescence study of  $(\text{C}_4\text{H}_9\text{NH}_3)_2\text{PbI}_4$  organic-inorganic quantum well, *J. Phys. Chem. C* **122**, 26623 (2018).
- [36] F. L. Lederman and J. D. Dow, Theory of electroabsorption by anisotropic and layered semiconductors. I. Two-dimensional excitons in a uniform electric field, *Phys. Rev. B* **13**, 1633 (1976).
- [37] T. Ishihara, J. Takahashi, and T. Goto, Optical properties due to electronic transitions in Two-dimensional semiconductors, *Phys. Rev. B* **42**, 11099 (1990).
- [38] K. Tanaka, T. Takahashi, T. Kondo, K. Umeda, K. Ema, T. Umabayashi, K. Asai, K. Uchida, and N. Miura, Electronic and excitonic structures of inorganic-organic perovskite-type quantum-well crystal  $(\text{C}_4\text{H}_9\text{NH}_3)_2\text{PbBr}_4$ , *Jpn. J. Appl. Phys.* **44**, 5923 (2005).
- [39] D. H. Cao, C. C. Stoumpos, T. Yokoyama, J. L. Logsdon, T.-B. Song, O. K. Farha, M. R. Wasielewski, J. T. Hupp, and M. G. Kanatzidis, Thin films and solar cells based on semiconducting two-dimensional Ruddlesden-Popper  $(\text{CH}_3(\text{CH}_2)_3\text{NH}_3)_2(\text{CH}_3\text{NH}_3)_{n-1}\text{Sn}_n\text{I}_{3n+1}$  perovskites, *ACS Energy Lett.* **2**, 982 (2017).
- [40] J. Ogle, D. Powell, E. Amerling, D.-M. Smilgies, and L. Whittaker-Brooks, Quantifying multiple crystallite orientations and crystal heterogeneities in complex thin film materials, *CrystEngComm* **21**, 5707 (2019).
- [41] P. Umari, E. Mosconi, and F. De Angelis, Infrared dielectric screening determines the Low exciton binding energy of metal-halide perovskites, *J. Phys. Chem. Lett.* **9**, 620 (2018).
- [42] M. Hirasawa, T. Ishihara, T. Goto, K. Uchida, and N. Miura, Magnetoabsorption of the lowest exciton in perovskite-type compound  $(\text{CH}_3\text{NH}_3)\text{PbI}_3$ , *Phys. B* **201**, 427 (1994).
- [43] D. B. Straus, S. Hurtado Parra, N. Iotov, J. Gebhardt, A. M. Rappe, J. E. Subotnik, J. M. Kikkawa, and C. R. Kagan, Direct observation of electron-phonon coupling and slow vibrational relaxation in organic-inorganic hybrid perovskites, *J. Am. Chem. Soc.* **138**, 13798 (2016).
- [44] N. Zibouche and M. S. Islam, Structure-electronic property relationships of 2D Ruddlesden-Popper tin- and lead-based iodide perovskites, *ACS Appl. Mater. Interfaces* **12**, 15328 (2020).
- [45] In this report, the “field strength,” symbolically represented by  $F$ , refers to the magnitude of the “applied field” divided by the material’s dielectric value at the frequency of the modulating voltage.
- [46] W. Joseph, N. Pradhan, S. Singh, and D. N. Rao, Electroabsorption spectroscopy: A versatile tool to measure optical nonlinearities, *Curr. Sci.* **86**, 1283 (2004).
- [47] D. E. Aspnes and J. E. Rowe, Resonant nonlinear optical susceptibility: Electroreflectance in the low-field limit, *Phys. Rev. B* **5**, 4022 (1972).
- [48] D. B. Mitzi, C. D. Dimitrakopoulos, and L. L. Kosbar, Structurally tailored organic-inorganic perovskites: Optical properties and solution-processed channel materials for thin-film transistors, *Chem. Mater.* **13**, 3728 (2001).
- [49] Y. Chen, Y. Sun, J. Peng, J. Tang, K. Zheng, and Z. Liang, 2D Ruddlesden-Popper perovskites for optoelectronics, *Adv. Mater.* **30**, 1703487 (2018).
- [50] E. A. Muljarov, S. Tikhodeev, N. Gippius, and T. Ishihara, Excitons in self-organized semiconductor/insulator superlattices: PbI-based perovskite compounds, *Phys. Rev. B* **51**, 14370 (1995).

- [51] M. I. Dar, G. Jacopin, S. Meloni, A. Mattoni, N. Arora, A. Boziki, S. M. Zakeeruddin, U. Rothlisberger, and M. Grätzel, Origin of unusual bandgap shift and dual emission in organic-inorganic lead halide perovskites, *Sci. Adv.* **2**, e1601156 (2016).
- [52] G. Weiser, Stark effect of One-dimensional wannier excitons in polydiacetylene single crystals, *Phys. Rev. B* **45**, 14076 (1992).
- [53] K. Miyata, T. L. Atallah, and X.-Y. Zhu, Lead halide perovskites: Crystal-liquid duality, phonon glass electron crystals, and large polaron formation, *Sci. Adv.* **3**, e1701469 (2017).
- [54] Z. Zhang, W.-H. Fang, M. V. Tokina, R. Long, and O. V. Prezhdo, Rapid decoherence suppresses charge recombination in multi-layer 2D halide perovskites: Time-domain ab initio analysis, *Nano Lett.* **18**, 2459 (2018).
- [55] G. Lanzani, *The Photophysics Behind Photovoltaics and Photonics* (Wiley-VCH, Weinheim, Germany, 2012).
- [56] T. G. Pedersen, H. Mera, and B. K. Nikolić, Stark effect in low-dimensional hydrogen, *Phys. Rev. A* **93**, 013409 (2016).
- [57] T. G. Pedersen, S. Latini, K. S. Thygesen, H. Mera, and B. K. Nikolić, Exciton ionization in multilayer transition-metal dichalcogenides, *New J. Phys.* **18**, 073043 (2016).
- [58] T. G. Pedersen, Exact polarizability of low-dimensional excitons, *Solid State Commun.* **141**, 569 (2007).
- [59] A. H. Proppe, *et al.*, Transition dipole moments of  $n = 1, 2$ , and 3 perovskite quantum wells from the optical Stark effect and many-body perturbation theory, *J. Phys. Chem. Lett.* **11**, 716 (2020).
- [60] F. Wang, J. Shan, M. A. Islam, I. P. Herman, M. Bonn, and T. F. Heinz, Exciton polarizability in semiconductor nanocrystals, *Nat. Mater.* **5**, 861 (2006).
- [61] D. E. Aspnes, Electric-Field effects on optical absorption near thresholds in solids, *Phys. Rev.* **147**, 554 (1966).
- [62] G. Weiser, A. Horvath, and H. Kolbe, in *Franz-Keldysh Effect of Band States in Polydiacetylene* (SPIE, 1997), Vol. 3145, Optical Science, Engineering and Instrumentation.
- [63] Y. Hamakawa, F. A. Germano, and P. Handler, Interband electro-optical properties of germanium. I. electroabsorption, *Phys. Rev.* **167**, 703 (1968).
- [64] M. E. Ziffer, J. C. Mohammed, and D. S. Ginger, Electroabsorption spectroscopy measurements of the exciton binding energy, electron-hole reduced effective mass, and band gap in the perovskite  $\text{CH}_3\text{NH}_3\text{PbI}_3$ , *ACS Photonics* **3**, 1060 (2016).
- [65] I. W. H. Oswald, A. A. Koegel, and J. R. Neilson, General synthesis principles for Ruddlesden-Popper hybrid perovskite halides from a dynamic equilibrium, *Chem. Mater.* **30**, 8606 (2018).
- [66] Z. Jiang, Gixsgui : A matlab toolbox for grazing-incidence X-ray scattering data visualization and reduction, and indexing of buried three-dimensional periodic nanostructured films, *J. Appl. Crystallogr.* **48**, 917 (2015).
- [67] M. Liess, S. Jeglinski, Z. Vardeny, M. Ozaki, K. Yoshino, Y. Ding, and T. Barton, Electroabsorption spectroscopy of luminescent and nonluminescent  $\Pi$ -conjugated polymers, *Phys. Rev. B* **56**, 15712 (1997).
- [68] S. A. Jeglinski, Ph.D. thesis, The University of Utah, 1996.
- [69] X. Zhang, Ph.D. thesis, North Carolina State University, 2006.
- [70] R. Elliott, Intensity of optical absorption by excitons, *Phys. Rev.* **108**, 1384 (1957).
- [71] I. Galbraith, Excitonic electroabsorption and electrorefraction in semiconductors, *Phys. Rev. B* **48**, 5105 (1993).
- [72] B. Numerov, *Publ. observatoire central astrophys.* Russ **2**, 188 (1933).
- [73] J. Cooley, An improved eigenvalue corrector formula for solving the Schrödinger equation for central fields, *Math. Comput.* **15**, 363 (1961).
- [74] W. Liptay, W. Eberlein, H. Weidenberg, and O. Elflein, Die beeinflussung der optischen absorption von molekülen durch ein äußeres elektrisches feld. V. Übergangsmomentrichtungen und dipolmomente der niedrigen elektronenzustände in 4-nitranilin, 1-nitro-3,5-diaminobenzol, 3,5-dinitroanilin, carbazol und 3,6-dinitrocarbazol, *Ber. Bunsen-Ges. Phys. Chem.* **71**, 548 (1967).
- [75] S. V. Novikov, D. H. Dunlap, V. M. Kenkre, P. E. Parris, and A. V. Vannikov, Essential Role of Correlations in Governing Charge Transport in Disordered Organic Materials, *Phys. Rev. Lett.* **81**, 4472 (1998).
- [76] J. Kang and L.-W. Wang, Dynamic disorder and potential fluctuation in two-dimensional perovskite, *J. Phys. Chem. Lett.* **8**, 3875 (2017).
- [77] Z. Zhang, W.-H. Fang, R. Long, and O. V. Prezhdo, Exciton dissociation and suppressed charge recombination at 2D perovskite edges: Key roles of unsaturated halide bonds and thermal disorder, *J. Am. Chem. Soc.* **141**, 15557 (2019).
- [78] M. Koecher, J. D. Yeager, T. Park, D. Fullwood, J. S. Colton, N. Mara, and N. Hansen, Characterization of nickel nanostrand nanocomposites through dielectric spectroscopy and nanoindentation, *Polym. Eng.* **53**, 2666 (2013).
- [79] M. W. den Otter, Approximate expressions for the capacitance and electrostatic potential of interdigitated electrodes, *Sens. Actuators, A* **96**, 140 (2002).
- [80] C. E. McClure, K. R. Hansen, L. Whittaker-Brooks, and J. S. Colton, Dielectric Spectroscopy on 2D and 3D Metal Halide Perovskites Using an Interdigitated Electrode Geometry To be published (2021).
- [81] Y. Shao, *et al.*, Grain boundary dominated ion migration in polycrystalline organic-inorganic halide perovskite films, *Energy Environ. Sci.* **9**, 1752 (2016).